Chemosphere 327 (2023) 138469

Contents lists available at ScienceDirect

Chemosphere

journal homepage: www.elsevier.com/locate/chemosphere

Boosting elimination of sunscreen, Tetrahydroxybenzophenone (BP-2), from water using monopersulfate activated by thorny NanoBox of Co@C prepared via the engineered etching strategy: A comparative and mechanistic investigation

Ta Cong Khiem [a], Nguyen Nhat Huy [b,c], Tran Doan Trang [a], Jet-Chau Wen [d], Eilhann Kwon [e], Hou-Chien Chang [f], Chechia Hu [g,**], Xiaoguang Duan [h], Kun-Yi Andrew Lin [a,*]

[a] Department of Environmental Engineering & Innovation and Development Center of Sustainable Agriculture, National Chung Hsing University, Taichung, 402, Taiwan
[b] Faculty of Environment and Natural Resources, Ho Chi Minh City University of Technology (HCMUT), Ho Chi Minh City, 700000, Viet Nam
[c] Vietnam National University Ho Chi Minh City, Ho Chi Minh City, 700000, Viet Nam
[d] National Yunlin University of Science and Technology, Douliu, Yunlin County, Taiwan
[e] Department of Earth Resources and Environmental Engineering, Hanyang University, SeongDong-Gu, Seoul, Republic of Korea
[f] Department of Chemical Engineering, National Chung Hsing University, Taichung, 402, Taiwan
[g] Department of Chemical Engineering, National Taiwan University of Science and Technology, Da'an Dist., Taipei City, 106, Taiwan
[h] School of Chemical Engineering and Advanced Materials, The University of Adelaide, SA, 5005, Australia

HIGHLIGHTS

- The sunscreen, Tetrahydroxybenzophenone (BP-2), is degraded by AOPs for the first time.
- BP-2 degradation can be boosted by Thorny Nanobox of Co@C with MPS.
- BP-2 degradation is comprehensively studied under various aquatic conditions.
- BP-2 degradation pathway is explored by theoretical and experimental evidences.

GRAPHICAL ABSTRACT

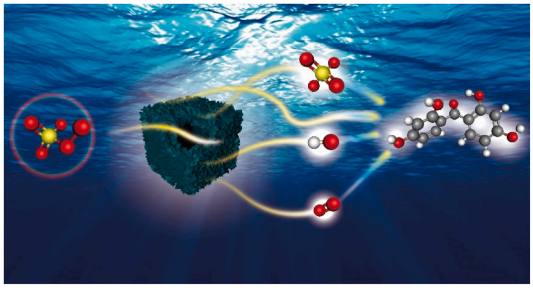

ARTICLE INFO

Handling editor: Sergi Garcia-Segura

Keywords:
Cobalt
Etching
Hollow
Nitrogen-doped carbon
MPS activation
BP-2

ABSTRACT

As sunscreens, benzophenones (BPs), are regarded as emerging contaminants, most of studies are focused on removal of 2-hydroxy-4-methoxybenzophenone (BP-3), which, however, has been employed for protecting skin. Another major class of BPs, which is used to prevent UV-induce degradation in various products, is completely neglected. Thus, this present study aims to develop a useful advanced oxidation process (AOP) for the first time to eliminate such a class of BP sunscreens from contaminated water. Specifically, 2,2′,4,4′-Tetrahydroxybenzophenone (BP-2) would be focused here as BP-2 is intensively used in perfumes, lipsticks, and plastics for preventing the UV-induced degradation. As monopersulfate (MPS)-based AOP is practical for degrading emerging contaminants, a facile nanostructured cobalt-based material is then developed for maximizing catalytic

* Corresponding author.
** Corresponding author.
E-mail addresses: chechia@mail.ntust.edu.tw (C. Hu), linky@nchu.edu.tw (K.-Y.A. Lin).

https://doi.org/10.1016/j.chemosphere.2023.138469
Received 9 February 2023; Received in revised form 14 March 2023; Accepted 19 March 2023
Available online 22 March 2023

activities of MPS activation by immobilizing Co nanoparticles onto carbon substrates. In particular, ZIF-67 is employed as a template, followed by the etching and carbonization treatments to afford the thorny nanobox of Co@C (TNBCC) with the hollow-nanostructure. In comparison to the solid (non-hollow) nanocube of Co@C (NCCC) from the direct carbonization of ZIF-67, TNBCC possesses not only the excellent textural features, but also superior electrochemical properties and highly reactive surfaces, making TNBCC exhibit the significantly higher catalytic activity than NCCC as well as Co_3O_4 in activating MPS to degrade BP-2. Mechanisms of BP-2 degradation are also elucidated and ascribed to both radical and non-radical routes. These advantageous features make TNBCC a useful catalyst of activating MPS in BP-2 degradation.

1. Introduction

While sunscreens are extensively added in sun protection products for protecting skin from the damage to UV irradiation (Jarry et al., 2004; Kim et al., 2011), sunscreens are also essential ingredients in various color and plastic products for preventing the UV-induced degradation (Jarry et al., 2004). Among all types of sunscreens, benzophenones (BPs) are the largest category in assorted products, and BPs and their derivative have been inevitably released to water bodies (Silvia Díaz-Cruz et al., 2008). Unfortunately, BPs have been proven as endocrine disrupting chemicals (EDCs), and could be accumulated within aquatic creatures and human body (Giokas et al., 2007). Thus, several methods, such as Fe(VI), UV/Cu_2WS_4/BiOCl, UV/H_2O_2, and UV/chlorine, have been developed so far to eliminate BPs from BP-polluted water. For example, in Fe(VI), the dioxygen transfer of Fe(VI) was proven to be responsible for 77.1% degradation of 10 μM BP-1 within 8 min with 100 μM Fe(VI) (Liu et al., 2022a). Meanwhile, 99% of 1 mg/L BP-1 could be degraded within 40 min under UV irradiation at over 420 nm with 20 mg 15% Cu_2WS_4/BiOCl in UV/Cu_2WS_4/BiOCl system. $^{\bullet}OH$ and $O_2^{\bullet-}$ were revealed as the main reactive species (Jiang et al., 2020). In the other two systems, BP-3 or BP-4 was employed as a target pollutant. For UV/H_2O_2, the degradation of BP-3 was ascribed to the generation of $^{\bullet}OH$, which enabled 62.93% of 0.1 mM BP-3 to be removed within 30 min with 0.05 M H_2O_2 under radiation of 14.22 Wm^{-2} at 254 nm (Gong et al., 2015). NaClO, on the other hand, was activated by UV to generate $^{\bullet}OH$, $Cl^{\bullet}$, and $Cl_2^{\bullet-}$ for BP-4 degradation in UV/chlorine system. 80% removal of 10 μM BP-4 was first observed after 10 s with 10 μM NaClO under UV radiation of 4.13 $mWcm^{-2}$ at 254 nm, but decreased to 36% after 5 min (Jia et al., 2019).

Overall, BPs can be degraded, but not effectively, and the concentration of BPs was too small. Therefore, it would be significant to find other methods for more efficient BP degradation. In this regard, monopersulfate (MPS) activation deserves attention as MPS, an inexpensive and environmentally benign oxidant, can generate the high-oxidation-power sulfate radicals ($SO_4^{\bullet-}$) to degrade refractory contaminants (Brillas and Martínez-Huitle, 2015; Zhang et al., 2015; Tuan et al., 2020a) as well as BPs effectively. To take one example, the complete degradation of 5 mg/L BP-1 was achieved within 35 min by CoFeNi nanoalloy@CNT-activated MPS, which contributed to the generation of $^{\bullet}OH/SO_4^{\bullet-}$ and $^1O_2$ as the main reason (Liu et al., 2023). In addition, total removal of 10 mg/L BP-4 obtained within 30 min with 100 mg/L NS-CNT-COOH and 1 g/L MPS (Liu et al., 2016) could be another example.

As 2,2′,4,4′-Tetrahydroxybenzophenone (BP-2) has been intensively used as a sunscreen in perfumes, lipsticks as well as plastics for packing of food (Jarry et al., 2004) to prevent the UV-induced degradation in these products, and BP-2 has been also validated to exhibit the strong endocrine disrupting activity (Jarry et al., 2004), it would be also useful to employ such promising MPS activation as abovementioned to eliminate BP-2 from wastewaters. However, the self-dissociation of MPS to generate $SO_4^{\bullet-}$ as well as other reactive oxygen species (ROS) is sluggish. Therefore, MPS must be activated by several methods, such as light, heat, and catalysts (Kohantorabi et al., 2021; Madihi-Bidgoli et al., 2021; Wang et al., 2022b; Zhang et al., 2022), for rapidly generating $SO_4^{\bullet-}$. Because of efficacy and convenience, heterogeneous catalysts have been confirmed as one of the most practical methods for activating MPS, and cobaltic catalysts have been proven to be the most useful materials for MPS activation in water (Tuan et al., 2022b, 2022c; Wang et al., 2022a). More importantly, no studies on employing Co-activated MPS in BP-2 degradation has ever conducted. Thus, it is highly-desired for developing advantageous Co-based materials to optimize MPS activation in degradation of BP-2.

As textural properties (e.g., surface areas and porosity) as well as surficial chemistry play decisive roles in activities of heterogeneous catalysts, nanostructured Co-based materials have been preferred for maximizing reactivities and, especially, immobilization of Co nanoparticles (NPs) onto carbonaceous substrates is also a promising strategy as the immobilization of Co NPs can enhance stability and robustness of Co NPs and the combination of Co and carbon also result in synergies for promoting catalytic activities (Tuan et al., 2021; Liu et al., 2022d, 2022e). Co@C, which allowed 5 mg/L diethyl phthalate to be degraded within 60 with 30 mg/L catalyst and 0.46 mM MPS, is a good example of this. The superior catalytic performance of Co@C was ascribed to the presence of abundant oxygen functional groups (Ma et al., 2022). Compared to solid Co@C, Co@C with hollow-structured carbon substrates possesses more advantages because of its favorability for decrease of the redundancy and creation of more surface areas, whereas magnetism would also enable heterogeneous catalysts to be easily manipulated and recovered (Khiem et al., 2022b; Tuan et al., 2022a). A recent study by DD Tuan et al. showed clearly this. The superior performance of HCoNC to SCoNC for bis(4-hydroxyphenyl) ketone degradation was mainly because of hollow structure (Tuan et al., 2022b). Therefore, a hollow-structured carbon-embedded Co with a high active area, porosity, and magnetism would be a promising activator for MPS to degrade BP-2 in water. To obtain such a hollow catalyst, etching strategy gains substantial interest. For instance, TC Khiem et al. employed tannic acid (TA) to fabricate HOCO with hollow structure. The resultant catalyst exhibited excellent performance for total degradation of 50 mg/L Azorubin S within 30 min with 100 mg/L HOCO/MPS. In another example, CoP/C-2 with high surface area of 32.2 m^2/g obtained from etching ZIF-67 with TA and followed by phosphorization also possessed a specific capacity of 104.5 mAh/g at 2 A/g, higher than that achieved by its counterpart without etching (Wang et al., 2023).

Herein, this study proposes a facile approach for developing such a catalyst by adopting Zeolitic Imidazolate Framework-67 (ZIF-67) as an initial precursor, followed by the etching treatment and carbonization to afford a thorny and hollow-structured nanobox (TNB) of cobalt embedded in carbon (Co@C) (denoted as TNBCC). This TNBCC exhibits a unique cubic and hollow morphology covered by thorny nanostructures, where cobalt (Co) NPs embedded throughout the carbonaceous matrices. Nitrogen dopant, derived from the carbonization of ZIF-67, can further improve conductivities and surficial activities of carbon, making TNBCC boost synergistic effects for improving catalytic activities towards MPS activation and then BP-2 degradation. Moreover, an analogue to TNBCC without the hollow structure as a solid-nanocube of Co@C (NCCC) is also prepared for comparing with TNBCC to investigate the structure-property relationship of such a hollow-engineered structure in activating MPS for BP-2 degradation. Besides, the mechanism of BP-2 degradation by TNBCC + MPS has been elucidated by determining ROS involved during BP-2 decomposition. Finally, the corresponding

decomposition process of BP-2 by TNBCC + MPS is also explored using experimental analysis and computer-aided investigations.

2. Experimental

2.1. Material preparation

All chemicals are acquired from major commercial sources (Text S1) and used directly. The template ZIF-67 was first fabricated according to previous study (Tuan et al., 2022b) using 1 mmol cobalt nitrate hexahydrate and 0.01 mmol cetyltrimethylammonium bromide (CTAB) dissolved in 10 mL of deionized (DI) water, which was then added dropwise into 70 mL of 0.8 M H-methylimidazole (HMIM). The mixture was stirred at room temperature for 1 h and the precipitation would be collected by centrifugation, washed by DI water/ethyl alcohol, and dried to afford the solid nanocube (NC) of ZIF-67. Subsequently, 300 mg ZIF-67 NC were immersed in 300 mL of DI water/ethyl alcohol (v/v = 1/1) containing 300 mg gallic acid (GA) while stirring for 10 min to allow the etching of ZIF-67. The resultant etched product was then collected and rinsed with ethyl alcohol before drying in an oven at 80 °C overnight, followed by a carbonization process in N_2 at 600 °C for 4 h to afford TNBCC. The solid ZIF-67 NC without etching was also carbonized via the same protocol for comparisons with TNBCC, and the resulting product of solid NC of Co@C would be denoted as NCCC.

2.2. BP-2 degradation procedures

BP-2 degradation using TNBCC coupled MPS was investigated by batch-type experiments. Firstly, 2.5 mg TNBCC was added to 100 mL of BP-2 solution with an initial concentration (C_0) of 10 mg/L for 30 min to examine the adsorption capability. Then, 20 mg MPS was instantly added to launch the degradation. At different reaction time t (min), an aliquot was taken out and passed through a filter to split off TNBCC from BP-2 solution. The concentration of BP-2 at t min (C_t) was subsequently measured at 275 nm using an UV–vis spectrophotometer. The effects of different parameters (catalyst/MPS dosage, temperature, pH, waters, co-existing components, and inhibitors) on BP-2 degradation were thoroughly examined. The recyclability of TNBCC for multiple BP-2 degradation cycles was performed by re-employing the used TNBCC (collected from 1 L of 10 mg/L BP-2 containing 25 mg TNBCC and 200 mg MPS in the first cycle) after filtration and drying at 80 °C. The rate constant (k) of BP-2 degradation was calculated using the pseudo-1st order equation:

$$C_t = C_0 \exp(-kt) \quad (1)$$

Other analytical protocols (ROS quantification, MPS decomposition, EPR measurement) and parameters for DFT calculation would be given in the supplementary material (Texts S3–S5 and Text S7).

2.3. Electrochemical analyses

The electrochemical analyses were measured on an electrochemical workstation (Potentiostat, CHI 621D) using a Pt wire as the counter electrode, an Ag/AgCl electrode as the reference electrode, and 20 μL of active suspension dropping on the glass carbon electrode (GCE) as the working electrode. The suspension was consisted of 16 mg catalysts, 2 mg carbon black, and 2 mg polyvinylidene fluoride in 10 mL of 1-Methyl-2-pyrrolidone dispersed ultrasonically for 1 h. KOH (1 M, 10 mL), which can offer ions and assure the reversible chemical reaction, was used as an electrolyte. The cyclic voltammetry (CV) was operated at 100 mV/s, while 5-mV scan rate was used to obtain the linear sweep voltammogram (LSV) curves, and the electrochemical impedance spectroscopy (EIS) was detected by applying a frequency from 100,000 Hz–0.01 Hz to with a 5-mV amplitude. Finally, the potentiodynamic polarization curves were recorded in the range of −0.6 to 0.6 V vs. Ag/AgCl at 10 mV/s. The overpotential (in V vs. RHE) was calculated using the following equation (Khiem et al., 2023b):

$$\eta = E_{RHE} - 1.23 = E_{Ag/AgCl} + 0.1976 + 0.0592 \times pH - 1.23 \quad (2)$$

For detection of electron transfer, the same procedures were adopted, but 0.5 M Na_2SO_4 was used as an electrolyte (see Text S6).

3. Results and discussion

3.1. Morphologies and compositional analyses

The fabrication of TNBCC using ZIF-67 as a template, followed by the etching treatment using gallic acid (GA) and then carbonization was illustrated in Fig. 1(a). The morphology of ZIF-67 was firstly examined in Fig. 1(b and c), revealing ZIF-67 with a cubic shape was obtained. Its XRD (Fig. 2(a)) was also well-indexed to the typical ZIF (Khiem et al., 2023a), further confirming the successful formation of ZIF-67. Once such a cubic ZIF-67 was carbonized, its cubic morphology with the solid structure can be retained as shown in Fig. 1(d and e); however, its surfaces had become roughened owing to the appearance of nanoparticles (Fig. 1(d)). Fig. 2(b) depicts that this resulting product merely contained Co, C and a slight amount of O without other elements, validating that Co was still preserved. Nevertheless, its crystalline structure (Fig. 2(a)) had become completely distinct from that of ZIF-67, indicating that the structure of ZIF-67 was entirely changed. In particular, the resultant product of the carbonization of ZIF-67 resulted in a few peaks at 26.1°, 44.1°, 51.4°, and 75.9°. The peak at 26.1° was ascribed to C, possibly resulted from pyrolysis of ligands, whereas the peaks at 44.1°, 51.4°, and 75.9° would be ascribed to (111), (200), and (220) planes of Co^0 (JCPDS#00-901-0968), suggesting that those NPs (Fig. 1(c)) could be cobaltic NPs, affording a nanocube (NC) of Co@C (NCCC).

On the other hand, when ZIF-67 received the etching treatment, interestingly, its morphology, even though retaining the cubic configuration, had become tremendously distinct from NCCC as the resulting product after the etching and carbonization treatment exhibited the fluffy appearance (Fig. 1(f)). The transmission image (Fig. 1(g)) further validates that the resultant product still retained the well-defined cubic morphology but its exterior had been fully covered by thorny nanostructures. More importantly, the solid structure of the origin ZIF-67 had disappearance and become hollow, affording a thorny nanobox (TNB). Fig. 2(b) further reveals the content in this TNB, and merely Co, C, as well as O were observed, which was comparable to NCCC. Besides, the XRD pattern of this TNB (Fig. 2(a)) contains a series of peaks at 44.1°, 51.4°, and 75.9°, attributed to carbon and Co^0. Therefore, the dark-colored NPs of TNB might be ascribed to Co NPs which distributed over the carbon substrate, forming the TNB of Co@C (TNBCC). On the other hand, an addition peak at 36.6° can be found in this TNBCC, corresponding to the (001) plane of CoO (JCPDS#00-153-3087). Different from NCCC, the appearance of CoO in TNBCC might occur because the hollow structure, maximizing the exposure of TNBCC to oxygen and causing a slight oxidation of Co NPs to afford CoO. Fig. S1 further shows the elemental mapping analyses of TNBCC, in which signals of carbon, oxygen as well as cobalt were uniformly distributed over those TNBCC particles.

3.2. Raman spectral analyses

In addition, Raman spectrum of TNBCC is measured in Fig. 2(c), showing a series of bands at 191, 475, 646, 1330 and 1586 cm^{-1}. The bands at 191, 475, and 646 cm^{-1} would correspond to cobalt species in Co^0 and CoO (Lin et al., 2017; Lai et al., 2018; Tuan et al., 2020b; Li et al., 2021), whereas the peak at 1330 as well as 1586 cm^{-1} could be then ascribed to the D-band and G-band of carbon (Lin et al., 2017; Lai et al., 2018; Tuan et al., 2020b; Li et al., 2021), respectively. These results further validate the existence of Co and carbonaceous substrate in TNBCC. On the other hand, the Raman spectrum of NCCC also showed the similar profile in which the peaks at 191, 475, 646, 1330 and 1586

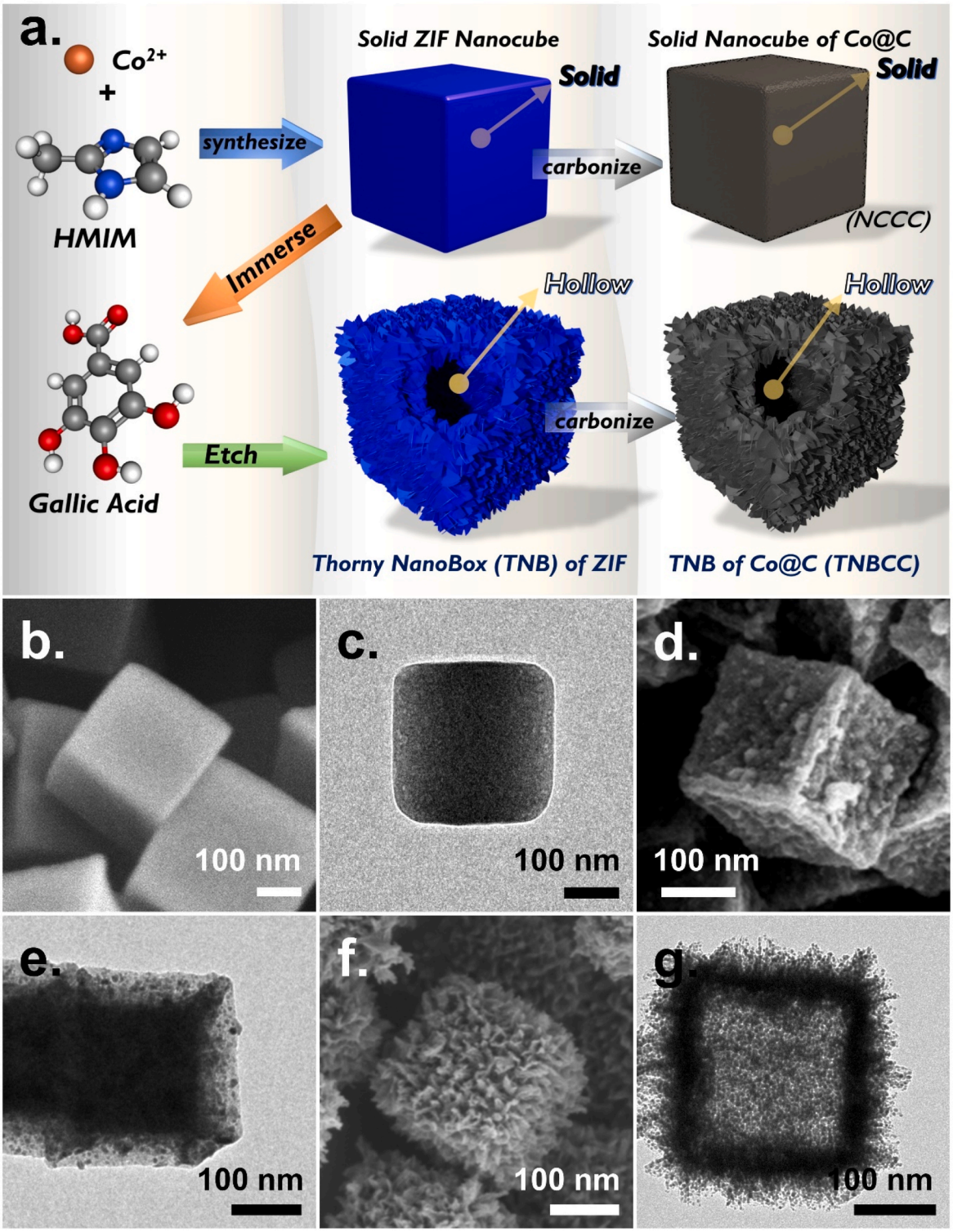

Fig. 1. (a) Preparation scheme of TNBCC and NCCC from ZIF-67; (b–g) images of (b, c) pristine ZIF-67, (d, e) NCCC, and (f, g) TNBCC.

cm^{-1} can be also observed without other noticeable signals. Nevertheless, one may note that the peak intensity ratio of I_D/I_G of TNBCC (i.e., 1.33) seemed larger than the ratio of I_D/I_G of NCCC (i.e., 1.20), suggesting that TNBCC contained more defects in its carbonaceous structure than NCCC. Since ZIF-67 is comprised of HMIM, the carbonization of HMIM in ZIF-67 actually would result in nitrogen-dopant into the carbonaceous substrate. Previous studies have reported that the introduction of N dopant into carbon would increase more defects (Wei et al., 2019); therefore, a higher I_D/I_G ratio in TNBCC might also suggest the N dopant in TNBCC might be more abundant (Wei et al., 2019). The hetero-atom doping and defects in the carbonaceous substrate have been also reported to enhance catalytic activities especially for oxidative reactions (Wei et al., 2019). This disordered carbon structure may result in more defects, that could be beneficial for enhancing redox reactions and boosting activities (Xue et al., 2021; Khiem et al., 2023b). Therefore, these results of Raman spectral analyses would suggest that TNBCC

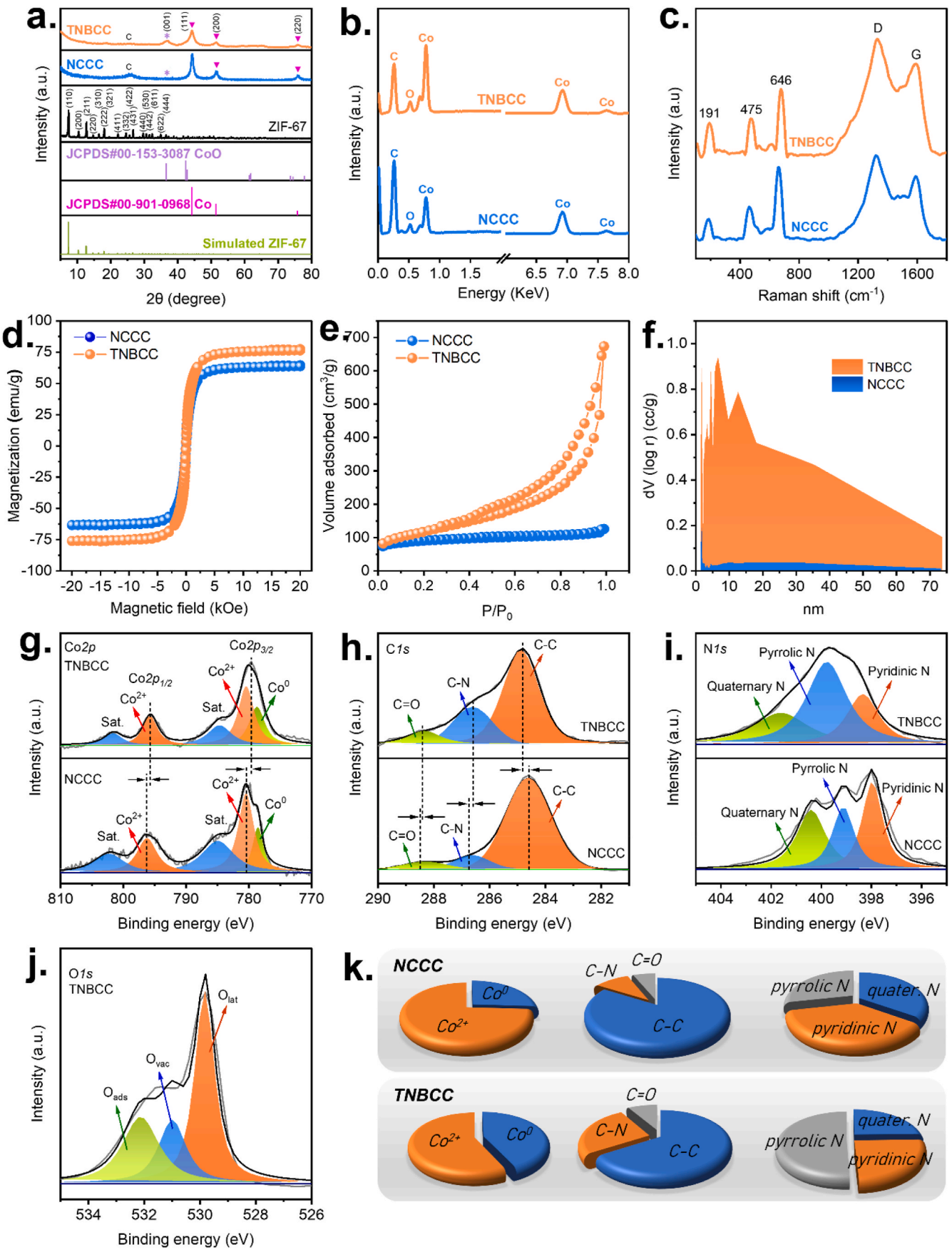

Fig. 2. Characterization of TNBCC and NCCC: (a) XRD, (b) EDS, (c) Raman, (d) magnetization, (e) N_2 sorption isotherms, (f) pore size distributions, (g–j) XPS, and (k) corresponding fractions of species.

might exhibit higher catalytic activity than NCCC for degradation of contaminants.

3.3. Magnetic and textural properties

Since TNBCC and NCCC both contained Co^0, enabling them to be magnetic, their magnetization would be analyzed. From −20 to +20 kOe, TNBCC revealed a very high magnetization of 75 emu/g (Fig. 2(d)), whereas NCCC displayed a less strong magnetization of 62 emu/g. These results validate that TNBCC is highly magnetic and can be easily manipulated under magnetic fields. The noticeably higher magnetization of TNBCC than NCCC might be also owing to the hollow structure with the void interior in TNBCC, allowing TNBCC to have less redundancy.

On the other hand, as TNBCC showed the interesting and unique thorny surface with the hollow boxed structure, its textural characteristics would be also analyzed in Fig. 2(e), in which the amount of N_2 adsorbed to TNBCC was significant with a huge hysteresis loop, suggesting that TNBCC shall exhibit a high surface area with abundant pores, especially mesopores as depicted in Fig. 2(f). The surface area of TNBCC was 412 cm^2/g with a porosity as 0.99 cc/g. Nonetheless, the amount of N_2 adsorbed to NCCC was significantly lower as shown in Fig. 2(e) with a very low porosity was obtained (Fig. 2(f)) possibly because of the solid structure and relatively flat surfaces of NCCC. Therefore, NCCC only showed 287 cm^2/g with a porosity of 0.06 cc/g. These comparisons also confirm that the etching treatment would enable TNBCC for revealing a much more advantageous surficial properties, especially the porous structures, which would maximize its active surface for catalytic activation of MPS.

3.4. Surface chemistry

The surface chemistry of heterogeneous catalysts also plays an important role for MPS activation. Thus, it shall be informative to probe into surface chemistry of NCCC and TNBCC. To this end, XPS analyses of these two catalysts were conducted and shown in Fig. 2(g–j). In Co*2p*, the spectrum of NCCC displays multiple bands at 778.5, 781.5 and 796.4 eV. The band at 778.5 eV corresponded to Co^0, while the bands at 781.5 as well as 796.4 eV correspond to Co^{2+} (Cao et al., 2020). The presence of these cobaltic species implies the partial oxidation on the surface of NCCC. Next, the C*1s* spectrum could be then deconvoluted into three underlying bands at 284.6 eV, 286.6 eV, and 288.3 eV, that were attributed to the C–C, C–N, and C═O bonds, respectively (Wang and Wang, 2021). This result also validates that nitrogen was doped onto carbon, derived from the carbonization of HMIM. Through the N doping onto carbon, the carbon matrix then exhibited defects as discussed in the earlier section of Raman analyses. Thus, the N*1s* peak can be also observed in NCCC as shown in Fig. 2(i), and it would reveal multiple peaks of N species at 399.6 eV, 401 eV, and 402.9 eV, corresponding to the pyridinic N, pyrrolic N, and quaternary N, respectively (Cao et al., 2020). This result also demonstrates that nitrogen was doped onto carbon via different routes to result in several nitrogenic species.

Similar to NCCC, the Co*2p*, C*1s*, and N*1s* spectra of TNBCC could be also deconvoluted to reveal the multiple bands. For instance, the Co*2p* spectrum contained Co^0 as well as Co^{2+}, whereas the C*1s* spectrum consisted of C–C, C–N and C═O, also confirming that carbon of TNBCC was doped with N. Thus, TNBCC also exhibited the N*1s* spectrum comprised of the pyridinic N, pyrrolic N, and quaternary N. Additionally, TNBCC exhibited a relatively noticeable peak of O*1s* (Fig. 2(j)) which can be then deconvoluted to reveal three underlying bands at 529.3, 530.5, as well as 531.7 eV, attributed to lattice O (O_{lat}), O vacancy (O_{vac}), and adsorbed O (O_{ads}), respectively (Chen et al., 2018; Liu et al., 2018; Khiem et al., 2022a).

While TNBCC and NCCC consisted of comparable surface chemical species, one can note that various species of each element were noticeably different. For instance, even though both catalysts contained Co^0 and Co^{2+}, the fraction of Co^0 in TNBCC (i.e., 43%) was considerably larger than that of Co^0 in NCCC (i.e., 26%) (Fig. 2(k)). As MPS activation would be initiated by the electron transfer, Co^0 is reported to provide additional electrons for mediate MPS activation (Andrew Lin et al., 2015, 2016; Lin et al., 2015; Andrew Lin and Chen, 2016). This might be also one of the possibilities that TNBCC exhibited more superior catalytic activity towards MPS activation and BP-2 degradation. The fraction of C–N species in TNBCC (i.e., 26%) was also much larger than that in NCCC (i.e., 10%), showing that TNBCC showed a higher degree of N-doping onto carbon, thereby resulting in more defects as revealed in Raman analyses earlier. More defects as well as the existence of the hetero-atom, N, would also create more catalytic sites, thereby enhancing the catalytic activity of TNBCC towards MPS activation (Lin et al., 2021; Trang et al., 2021).

In the case of N*1s* spectra, one can also notice that TNBCC showed quite distinct distribution of nitrogenic species as pyridinic N, pyrrolic N, quaternary N accounted for 25%, 51%, and 24%, respectively, whereas NCCC consisted of pyridinic N, pyrrolic N, quaternary N corresponding to 37%, 28%, and 35%, respectively. As both pyridinic N and pyrrolic N are validated as active sites for MPS activation (Miao et al., 2020), the sum of pyridinic N and pyrrolic N in TNBCC (i.e., 76%) was much higher than the sum of them in NCCC as 65%. As the fraction of C–N species in TNBCC was already much higher than that in NCCC, the relatively high fraction of pyridinic N and pyrrolic N in TNBCC shall enable TNBCC to exhibit much more active sites than NCCC, making TNBCC exhibit higher activities for activating MPS in BP-2 degradation.

Moreover, since TNBCC was also comprised of O_{vac} which has been also reported as a catalytic site for contributing to MPS activation (Khiem et al., 2022a; Liu et al., 2022f). Thus, these aforementioned comparisons clearly indicate that TNBCC, obtained from the etching treatment, possessed not only the unique morphology for improving its textural features, but also advantageous surficial properties as well as highly reactive surfaces, making TNBCC an excellent activator for MPS in BP-2 degradation.

3.5. Electrochemical analyses

As MPS activation is essentially a redox process between MPS and catalysts, electrochemical characteristics of catalysts would be the key to MPS activation (Liu et al., 2022b; Khiem et al., 2023a, 2023b). Thus, it would be insightful to examine differences in electrochemistry between TNBCC and NCCC. Fig. 3(a) shows CV curves of TNBCC and NCCC. While NCCC showed an insignificant peak current in this potential window, TNBCC exhibited several huge redox peaks with very large peak currents. Therefore, TNBCC could possess a noticeably larger specific capacitance (C_p) of 55.16 F/g than 27.58 F/g of NCCC (calculated via Eq. (3) using data in Fig. S2), confirming that TNBCC showed much greater redox properties and should enable the faster interfacial reaction rates than NCCC (Khiem et al., 2023a).

$$C = I \times \Delta t / (\Delta V \times m) \quad (3)$$

where I, Δt, ΔV, and m represent the discharge current (0.001 A), discharge time (2 s for NCCC and 4 s for TNBCC), charge and discharge voltage (~2.266 V vs. RHE), and mass of the electro-material on the electrode ($\sim 0.032 \times 10^{-3}$ g), respectively. This also demonstrates that TNBCC possessed much more reactive sites, possibly owing to its high porosities to provide a larger ion reservoir (Liu et al., 2022b; Khiem et al., 2023a) for minimizing the diffusion pathway and facilitating ionic diffusion (Jiang et al., 2014). From CV curves of TNBCC at different scan rates in Fig. 3(b), both anodic and cathodic peak current increased with the scan rate, suggesting the absorption-controlled behavior of TNBCC (Khiem et al., 2023b).

On the other hand, LSV curves of TNBCC as well as NCCC are also displayed in Fig. 3(c). At the current density = 10 mA/cm^2, an initial potential of 0.555 V was reached by TNBCC, whereas NCCC would

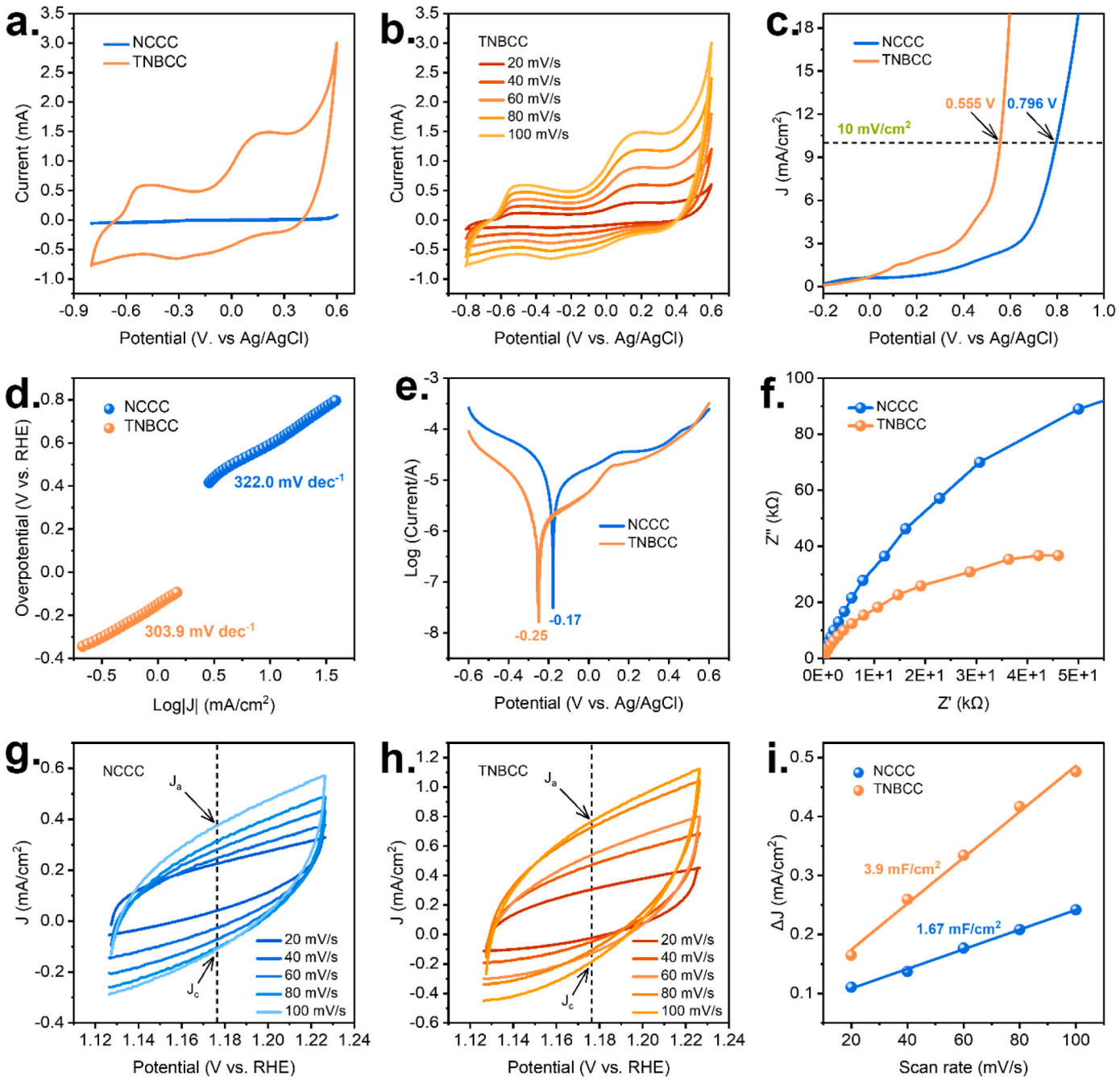

Fig. 3. Electrochemical properties of TNBCC and NCCC: (a) CV curves at 100 mV/s, (b) CV curves of TNBCC at different scan rate, (c) LSV curves at 5 mV/s, (d) Tafel plot at 10 mV/s, (e) potentiodynamic polarization curves, (f) EIS Nyquist plots, (g, h) CV curves of NCCC and TNBCC in the double layer capacitive region, and (i) ECSA curves with C_{DL} values (obtained from the slope of linear equation between ΔJ (= $|J_a| + |J_c|$)/2 and scan rate).

necessitate a much larger initial potential of 0.796 V, indicating that the electron transport process within TNBCC would be more efficient than NCCC. Furthermore, the corresponding Tafel slopes of TNBCC and NCCC are then summarized in Fig. 3(d), in which TNBCC exhibited a much lower Tafel slope of 303.9 mV/dec than that of NCCC as 322.0 mV/dec, suggesting that TNBCC would enable a much more efficient kinetic process than NCCC. Besides, their corresponding Tafel polarization curves were also measured in Fig. 3(e), revealing that the corrosion potential of TNBCC possessed a more negative corrosion potential of −0.25 V than that of NCCC (−0.17 V). A relatively negative corrosion potential has been related to a higher degree of electron transfer, which, in turn, facilitates activating MPS. Thus, TNBCC would be also expected to enable a higher degree of electron transfer, thereby boosting MPS activation and BP-2 degradation.

Additionally, the charge transfer behaviors of TNBCC and NCCC were also determined based on its Nyquist plot (Fig. 3(f)). In comparison to NCCC, TNBCC reveals a noticeable smaller semi-circle in the high-frequency zone, demonstrating that TNBCC would possess a higher charge transfer efficiency with a lower resistance (Li et al., 2018). Fig. 3 (i) further displays that TNBCC also possessed a considerably huger double layer capacitance (C_{DL}) of 3.9 mF/cm^2 than that of NCCC (1.67 mF/cm^2) based on a series of CV curves at various scan rates (Fig. 3(g and h)). The electrochemically active surface area (ECSA in cm^2) of these catalysts can be then calculated via Eq. (4) (Khiem et al., 2023b):

$$ECSA = S \times C_{DL}/C_s \quad (4)$$

Where S represents the working electrode area of $\pi \times 0.3^2/4$ cm^2 and C_s is the specific capacitance of an ideal electrode (i.e., 40×10^{-6} F/cm^2 in 1 M KOH). The corresponding ECSA of TNBCC would be then calculated as 6.89 cm^2, whereas NCCC only showed an ECSA of 2.95 cm^2, signifying that TNBCC exhibited a huger active surface than NCCC for the redox reactions during MPS activation.

More importantly, these results and textural properties suggest that the etching treatment by GA on ZIF-67 would not only modify the morphology of TNBCC by making it thorny and hollow to exhibit more surfaces and porosities, but also substantially enhance the electrochemical characteristics of TNBCC for promoting its catalytic activities towards MPS activation and BP-2 degradation.

3.6. Degradation of BP-2 by TNBCC + MPS system

The degradation of BP-2 via catalytic activation of MPS by TNBCC was examined in Fig. 4(a). First, it would be necessary to evaluate the adsorption of BP-2 onto TNBCC. In Fig. 4(a), the concentration of BP-2 was negligibly changed in the presence of TNBCC only, indicating that BP-2 was barely removed via adsorption. Also, it can be noticeable that almost no BP-2 was degraded when MPS alone was added, signifying that MPS itself could not effectively degrade BP-2. Nevertheless, once both of TNBCC and MPS were introduced, BP-2 concentration was significantly decreased and fully eliminated as its C_t/C_0 reached "0" within 20 min, indicating the superior reactivity of TNBCC for activating MPS to degrade BP-2 from water. For comparison, commercial Co_3O_4

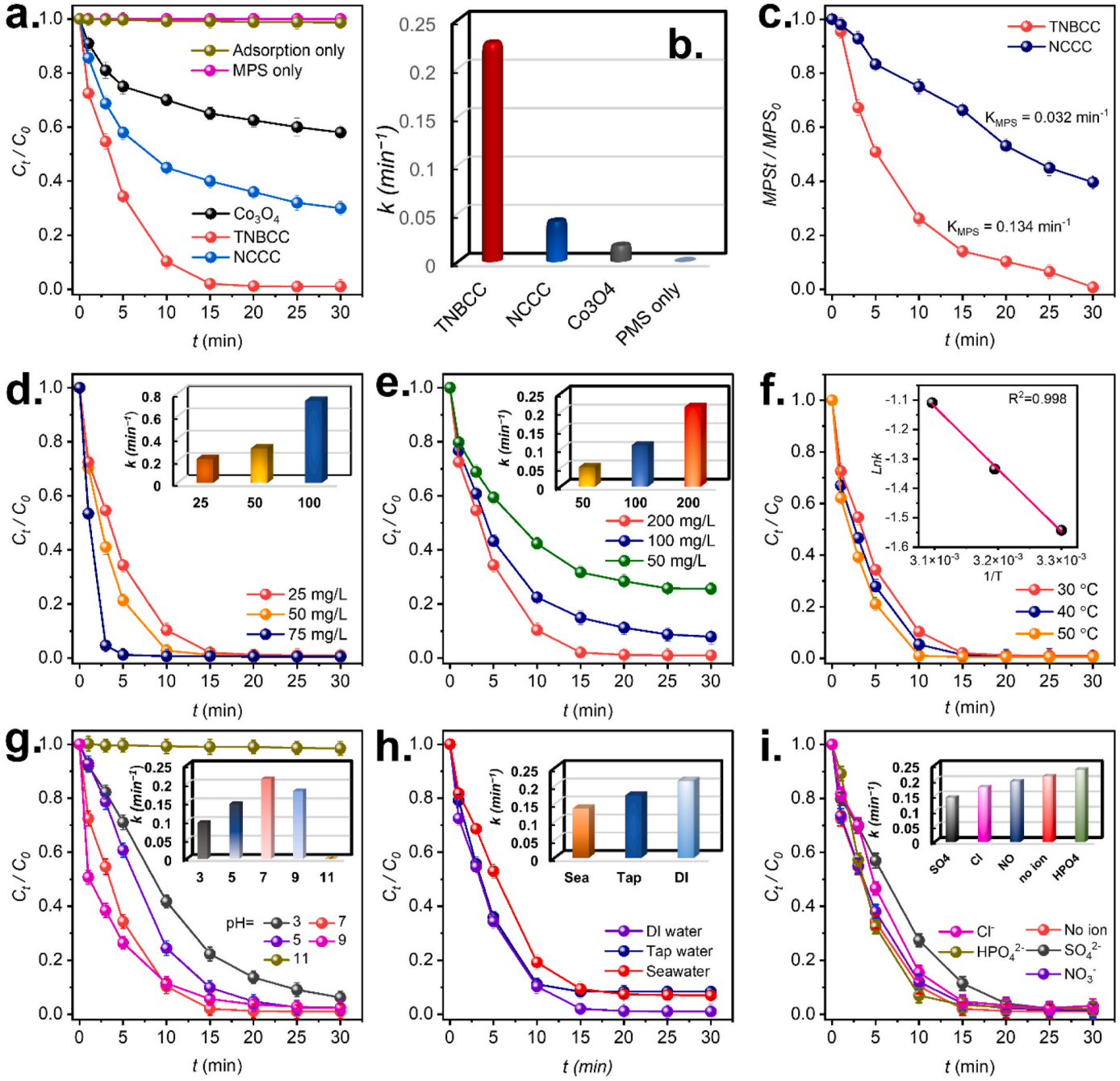

Fig. 4. (a) Comparison of degradation of BP-2 and (b) corresponding rate constants by various catalysts; (c) comparison of MPS consumption (catalysts = 25 mg/L, MPS = 200 mg/L, BP-2 = 10 mg/L, and T = 30 °C); (d–i) effects of various factors on BP-2 degradation by TNBCC + MPS: (d) TNBCC concentration, (e) MPS concentration, (f) temperature, (g) pH, (h) water matrices, and (i) anions (TNBCC = 25 mg/L, MPS = 200 mg/L, BP-2 = 10 mg/L, anions = 10 mM, and T = 30 °C).

NPs and NCCC were also employed to activate MPS for eliminating BP-2 in Fig. 4(a). Co_3O_4+MPS could reduce 35% of BP-2 whereas NCCC + MPS could eliminate 68% of BP-2. This result demonstrates that these cobaltic materials were also capable of activating MPS for BP-2 degradation; however, the BP-2 degradation efficiencies of these two catalysts were lower than that of TNBCC. The rate constants of BP-2 degradation using those aforementioned catalytic systems were also calculated by Eq. (1) and illustrated in Fig. 4(b). The rate constant (k) calculated from TNBCC + MPS system is 0.214 min^{-1}, which would be substantially higher than those of Co_3O_4+MPS (0.017 min^{-1}) and NCCC + MPS (0.042 min^{-1}), validating the superior activity of TNBCC.

As TNBCC enabled the much faster degradation of BP-2 than NCCC, it might be also insightful to examine how these two catalysts would activate (or utilize) MPS. Therefore, the concentration of MPS along the degradation of BP-2 had been monitored in Fig. 4(c), in which the concentration of MPS in the presence of TNBCC decreased very quickly as MPS was almost completely decomposed in the presence of TNBCC in 30 min. On the other hand, the consumption of MPS in the presence of NCCC seemed much slower and less quickly than that by TNBCC. The corresponding k of MPS consumption by TNBCC would be determined as 0.134 min^{-1}, whereas the k using NCCC would be 0.032 min^{-1}. These results validate that TNBCC can enable the quicker and more efficient MPS activation than NCCC, thereby leading to the much more effective BP-2 degradation. These results confirm that TNBCC showed a remarkable catalytic activity for activating MPS to degrade BP-2. More importantly, TNBCC with the hollow-engineered nanostructure exhibited the distinctive performance compared with the non-hollow engineered nanostructure NCCC, demonstrating the advantageous properties of the hollow structure in TNBCC for activation of MPS and elimination of BP-2 in water. Furthermore, TNBCC is also found to be more effective than the most recently reported catalysts for MPS activation in BP degradation as summarized in Table 1 below.

3.7. Other effects on BP-2 degradation

As TNBCC + MPS efficiently degraded BP-2, it was interesting to examine other parameters on BP-2 degradation. At first, the TNBCC concentration was varied in Fig. 4(d). At 25 mg/L of TNBCC, >90% of BP-2 was degraded in 10 min and the full degradation of BP-2 would be reached in 20 min. When the TNBCC dosage was increased to 50 mg/L, BP-2 was almost completely degraded in 15 min. At TNBCC = 75 mg/L, the full degradation of BP-2 was reached in a shorter reaction time within 10 min. The corresponding k at TNBCC = 25, 50, and 75 mg/L would be determined as 0.214, 0.308, and 0.736 min^{-1}, respectively, demonstrating that a higher TNBCC dosage led to the much faster BP-2 owing to the availability of more active sites. Moreover, such a result also suggests that a slight amount of TNBCC at 25 mg/L was already highly effective to enable the complete BP-2 degradation. The effect of MPS dosage, with TNBCC = 25 mg/L, is revealed in Fig. 4(e), in which a lower MPS dosage (e.g., 50 and 100 mg/L) would cause slower and incomplete BP-2 degradation and at least 200 mg/L of MPS was necessitated.

Furthermore, the effect of temperature would be also considered in Fig. 4(f), in which BP-2 degradation efficiencies and reaction rate constants would be substantially improved from 30 to 50 °C, revealing that the enhancing effect of higher temperatures on BP-2 degradation possibly owing to the facilitated mass transfer. Besides, the rate constants were then correlated to temperature to determine the activation energy of BP-2 degradation through the Arrhenius equation (Eq. (5)) (Chen et al., 2022; Liu et al., 2022c) as follows:

$$\ln k = \ln A - E_a/RT \quad (5)$$

where E_a is the activation energy (kJ/mol). In the inset of Fig. 4(f), the data points can be well-fitted (R^2 = 0.998), and the corresponding E_a was computed as 17.6 kJ/mol, which was much smaller than the recent reported studies of degradation of BP-based UV filters as summarized in Table S3, demonstrating that TNBCC is a highly advantageous catalyst of MPS activation to remove BP-based UV filters, such as BP-2.

The effect of pH on activating BP-2 by TNBCC + MPS would be investigated in Fig. 4(g). While the neutral condition at pH = 7 had allowed the quick BP-2 degradation, a relatively acidic condition at pH = 5 seemed to slow the BP-2 degradation as the k dropped marginally from 0.214 to 0.147 min^{-1}, but BP-2 was still fully degraded within 30 min. The more acidic condition at pH = 3 would lead to the even more adverse effect on BP-2 degradation with k = 0.097 min^{-1} and incomplete degradation within 30 min. This was possibly because the higher concentration of H^+ under the acidic condition might also act as a scavenger to consume $SO_4^{\bullet-}$ and $^{\bullet}OH$ via Eq. (6) and Eq. (7), thereby diminishing BP-2 degradation efficiency (Nguyen et al., 2021; Tuan et al., 2022b).

$$H^+ + {}^{\bullet}OH + e^- \rightarrow H_2O \quad (6)$$

$$H^+ + SO_4^{\bullet-} + e^- \rightarrow HSO_4^- \quad (7)$$

Moreover, MPS would become relatively indolent under the acidic condition (Guo et al., 2013), making MPS harder to be decomposed, hence resulting in the less efficient BP-2 elimination. In the case of the basic condition at pH = 9, BP-2 could be still efficiently degraded as BP-2 could be fully degraded within 30 min but the k seemed to become smaller as 0.180 min^{-1}. When pH was then adjusted to 11, the relatively basic condition, surprisingly, BP-2 was barely degraded, demonstrating that the strongly alkaline condition was disadvantageous to BP-2 degradation, possibly because the TNBCC surface would become more negative under the basic condition (Fig. S3), which in turn resulted in the more intensive electrostatic revulsion between BP-2 and TNBCC, and SO_5^{2-}, hence decreasing the degradation efficiency of BP-2 (Tuan et al., 2022a). Moreover, since the concentration of OH^- would increase under the basic condition, the probability of $SO_4^{\bullet-}$ reacting with OH^- would also increase to produce $^{\bullet}OH$, thus causing the lower efficacy.

In addition, since BP-2 is a popular UV absorber and may exist in various water bodies, it would be useful to further evaluate BP-2 degradation by TNBCC + MPS in different water matrices. Therefore, in addition to DI water, tap water and seawater containing BP-2 were then used as experimental media in Fig. 4(h). Interestingly, when tap water was used, the initial BP-2 degradation still remained very effective until 10 min with a k = 0.174 min^{-1}. As tap water actually consists of

Table 1
A summary of reported catalysts for MPS activation in BP degradation.

Catalyst (conc.)	MPS conc. (mg/L)	Pollutant (conc.)	Degradation time (min)	Removal (%)	Ref.
$CoFe_2O_4$ (100 mg/L)	200	4DHB (5 mg/L)	60	>90%	Khiem et al. (2022a)
Co_2TiO_4 (200 mg/L)	200	4DHB (5 mg/L)	20	100%	Mao et al. (2022)
HCoNC (100 mg/L)	150	4DHB (5 mg/L)	30	100%	Tuan et al. (2022b)
Nanoplate-assembled CoS (100 mg/L)	200	4DHB (5 mg/L)	60	100%	Liu et al. (2022g)
Cobalt sulfide nanofilm (50 mg/L)	100	4DHB (5 mg/L)	15	100%	Yin et al. (2021a)
CoFeNi@CNT (100 mg/L)	200	BP-1 (5 mg/L)	35	100%	Liu et al. (2023)
TNBCC (25 mg/L)	200	BP-2 (10 mg/L)	20	100%	**This study**

4DHB = 4,4′-Dihydroxybenzophenone (a member of BPs).

many impurities, such as ions and solids, the overall BP-2 degradation efficiency was satisfactory as > 90% of BP-2 could be degraded within 30 min. In the case of seawater, BP-2 could be still degraded by TNBCC + MPS even though the k was slightly lower as 0.138 min^{-1} given that seawater contains a significant number of impurities, especially salts and minerals. The less effective degradation in seawater and tap water might be because Cl^- would exist in these media, and Cl^- would consume radicals (such as $SO_4^{\bullet-}$) to become chloride radicals (i.e., $Cl^{\bullet}$, $Cl_2^{\bullet-}$) (Zhang et al., 2014) as follows (Eq. (8) and (9)).

$$SO_4^{\bullet-} + Cl^- \rightarrow SO_4^{2-} + Cl^{\bullet} \quad (8)$$

$$Cl^{\bullet} + Cl^- \rightarrow Cl_2^{\bullet-} \quad (9)$$

These Cl-based radical species exhibit lower oxidation potential than $SO_4^{\bullet-}$, thereby decreasing the degradation effectiveness of BP-2. Nevertheless, overall, TNBCC + MPS was still a useful and feasible approach even in the media of tap water and seawater for degrading BP-2.

As the presence of ions seemed to impact the BP-2 degradation, we then further investigated the effect of several common anions on BP-2 degradation in Fig. 4(i). Specifically, in the case of Cl^-, BP-2 degradation was certainly influenced as the k was lower to 0.178 min^{-1}, validating that the presence of Cl^- could cause negative effects because of occurrence of Cl radicals. When NO_3^- and SO_4^{2-} were present, these ions might also interfere with TNBCC to accumulate more negative charges on the surface of TNBCC, causing stronger repulsions between the catalyst and MPS, and therefore decreasing the degradation efficiency slightly. Nevertheless, in the case of HPO_4^{2-}, the BP-2 degradation was not significantly influenced as BP-2 was still quickly and completely degraded. This was possibly because phosphate ions have been reported to activate MPS (Wen et al., 2022) and thus the presence of HPO_4^{2-} might cause a slight enhancement in BP-2 degradation.

3.8. Reusability of TNBCC for multiple BP-2 degradation cycles

Since TNBCC + MPS could effectively degrade BP-2, the reusability and stability of TNBCC for continuously decomposing MPS in degrading BP-2 for repeated cycles were then examined. As shown in Fig. S4(a), it would be obviously noticed that BP-2 was still effectively degraded over 5 consecutive cycles without any significant changes using the used TNBCC. This result suggests that TNBCC remained very efficient for MPS activation for degrading BP-2. On the other hand, the surficial chemistry of used TNBCC would be analyzed in Figs. S4(b–d) for revealing its Co*2p*, C*1s* and N*1s* core-level spectra, respectively. Overall, these core-level spectra were very comparable to those of the pristine TNBCC. For instance, both Co^0 and Co^{2+} were both retained within TNBCC, whereas the C–N species was also preserved with the relatively high fractions of pyrrolic and pyridinic N species, demonstrating that TNBCC was a robust and stable heterogeneous catalyst as the catalytically-active species of TNBCC remained over the multiple cycles of BP-2 degradation.

3.9. Degradation mechanism by TNBCC + MPS

To identify ROS from TNBCC + MPS during BP-2 degradation, the effects of scavengers on BP-2 elimination were then explored. Specifically, methanol is adopted as an inhibitor for scavenging $SO_4^{\bullet-}$ ($k = 2.5 \times 10^7$ $M^{-1}s^{-1}$) and $^{\bullet}OH$ ($k = 9.7 \times 10^8$ $M^{-1}s^{-1}$), whereas tert-butanol (TBA) is used as an inhibitor for $^{\bullet}OH$ solely ($k = 3.8–7.6 \times 10^8$ $M^{-1}s^{-1}$) (Khiem et al., 2023b). In addition, the existence of O_{vac} in TNBCC could lead to the formation of singlet oxygen ($^1O_2$) via Eq. (11) after active oxygen (O*) was formed (Eq. (10)) (Khiem et al., 2022a).

$$O_{vac} \rightarrow O* \quad (10)$$

$$O* + HSO_5^- \rightarrow HSO_4^- + {}^1O_2 \quad (11)$$

Thus, sodium azide (NaN_3) was adopted to scavenge, $k = 1.0 \times 10^9$ $M^{-1}s^{-1}$). Fig. 5(a) displays that even though BP-2 was still fully degraded within 30 min in the presence of TBA, a relatively low k of 0.168 min^{-1} for BP-2 degradation was observed, signifying $^{\bullet}OH$ might be produced but accounted for a very minor contribution. Next, when methanol was introduced, BP-2 degradation was significantly suppressed and inhibited as C_t/C_0 in 30 min was merely 0.8 and k was only 0.006 min^{-1}, signifying that $SO_4^{\bullet-}$ and $^{\bullet}OH$ might both occur from TNBCC + MPS and $SO_4^{\bullet-}$ would be a dominant ROS. In addition, BP-2 degradation also became slower when NaN_3 was introduced into the solution as C_t/C_0 merely reached 0.7 in 30 min with a k of 0.008 min^{-1} (Fig. 5(b)), suggesting that $^1O_2$ might be also present from TNBCC + MPS, and BP-2 degradation was involved with the non-radical route. As reported in a previous study (Khiem et al., 2023b), $O_2^{\bullet-}$ might also be formed via the following equations.

$$HSO_5^- + H_2O \rightarrow H_2O_2 + HSO_4^- \quad (12)$$

$$Co(II) + HSO_5^- \rightarrow Co(III) + SO_4^{\bullet-} + OH^- \quad (13)$$

$$SO_4^{\bullet-} + H_2O_2 \rightarrow SO_4^{2-} + HO_2^{\bullet} + H^+ \ \left(k = 1.2 \times 10^7\ M^{-1}s^{-1} \text{ at pH } 7\right) \quad (14)$$

$$HO_2^{\bullet} \rightarrow H^+ + O_2^{\bullet-} \quad (15)$$

The effect of BQ on BP-2 elimination would, therefore, need to be investigated ($k = 2.9 \times 10^9$ $M^{-1}s^{-1}$). As a result, a noticeable inhibition against BP-2 degradation was seen as C_t/C_0 at 30 min merely reached 0.4 with k = 0.034 min^{-1}, manifesting that $O_2^{\bullet-}$ might be generated and contributed to BP-2 degradation.

To further confirm the existence of these ROS, EPR measurements were then implemented by DMPO and TEMP as two typical spin-trapping agents for capturing $^{\bullet}OH$, $SO_4^{\bullet-}$, $O_2^{\bullet-}$, and $^1O_2$. As can be seen in Fig. 5(c), no obvious EPR patterns were observed when MPS was individually added into either DMPO, while noticeable patterns of DMPO-$^{\bullet}OH$ and DMPO-$SO_4^{\bullet-}$ were observed once MPS was introduced into the mixture of DMPO and TNBCC (Tuan et al., 2020c). This confirms that $^{\bullet}OH$ and $SO_4^{\bullet-}$ were produced and contributed to BP-2 degradation. Moreover, the same procedure was repeated but in the medium of methanol to see if $O_2^{\bullet-}$ occurred in TNBCC + MPS. Nevertheless, only the signals of 5,5-dimethylpyrroline-(2)-oxyl-(1) (DMPOX), instead of DMPO-$O_2^{\bullet-}$, was observed, indicating either insignificant amount of $O_2^{\bullet-}$ was generated in TNBCC + MPS or the oxidation rate of DMPO by $O_2^{\bullet-}$ was faster than trapping rate, which is different from those in different MnO_2/MPS systems where the oxidation of DMPO in water by $^{\bullet}OH$ and $SO_4^{\bullet-}$ was believed to be the main reason (Huang et al., 2019). To prove this, further reduction of nitro blue tetrazolium chloride (NBT) by $O_2^{\bullet-}$ ($k = 5.76–6.04 \times 10^4$ $M^{-1}s^{-1}$) to form monoformazan at 530 nm on the UV–vis spectra was employed (Khiem et al., 2023c). However, Fig. 5(d) shows no peak of monoformazan at was found at 530 nm, suggesting the absence of $O_2^{\bullet-}$ in TNBCC + MPS The less effective BP-2 degradation observed in the case of the addition of BQ might be that fact that the introduction of BQ could consume more MPS without generation of useful ROS (Zhou et al., 2015) and also interfere the approach of MPS towards the surface of TNBCC (Khiem et al., 2022a). In contrast, an intensive 1:1:1 triplet pattern characteristic of TEMP-$^1O_2$ could be also observed when MPS combined with TEMP and TNBCC as displayed in Fig. 5(c), confirming the existence of $^1O_2$ (Zhu et al., 2022). These results further elucidate that BP-2 degradation using TNBCC + MPS was associated with multiple ROS, namely, the radical and non-radical route, and $SO_4^{\bullet-}$ shall serve as the dominant ROS to contribute to BP-2 degradation.

To further probe into the occurrence of these ROS, appearance of $SO_4^{\bullet-}$ and $^{\bullet}OH$ at different reaction times would be then quantified via the "semi-quantitative" analyses using particular probe agents (Yin et al., 2021b; Khiem et al., 2022a, 2023a, 2023b). As Fig. 5(e) signifies, the presence of $SO_4^{\bullet-}$ and $^{\bullet}OH$ validated by the formation of *para*-benzoquinone (*p*-BQ) and *para*-hydroxybenzoic acid (*p*-HPA), respectively suggested the levels of both $SO_4^{\bullet-}$ and $^{\bullet}OH$ rose up after a longer time interval. Nevertheless, the level of $SO_4^{\bullet-}$ appeared higher than $^{\bullet}OH$,

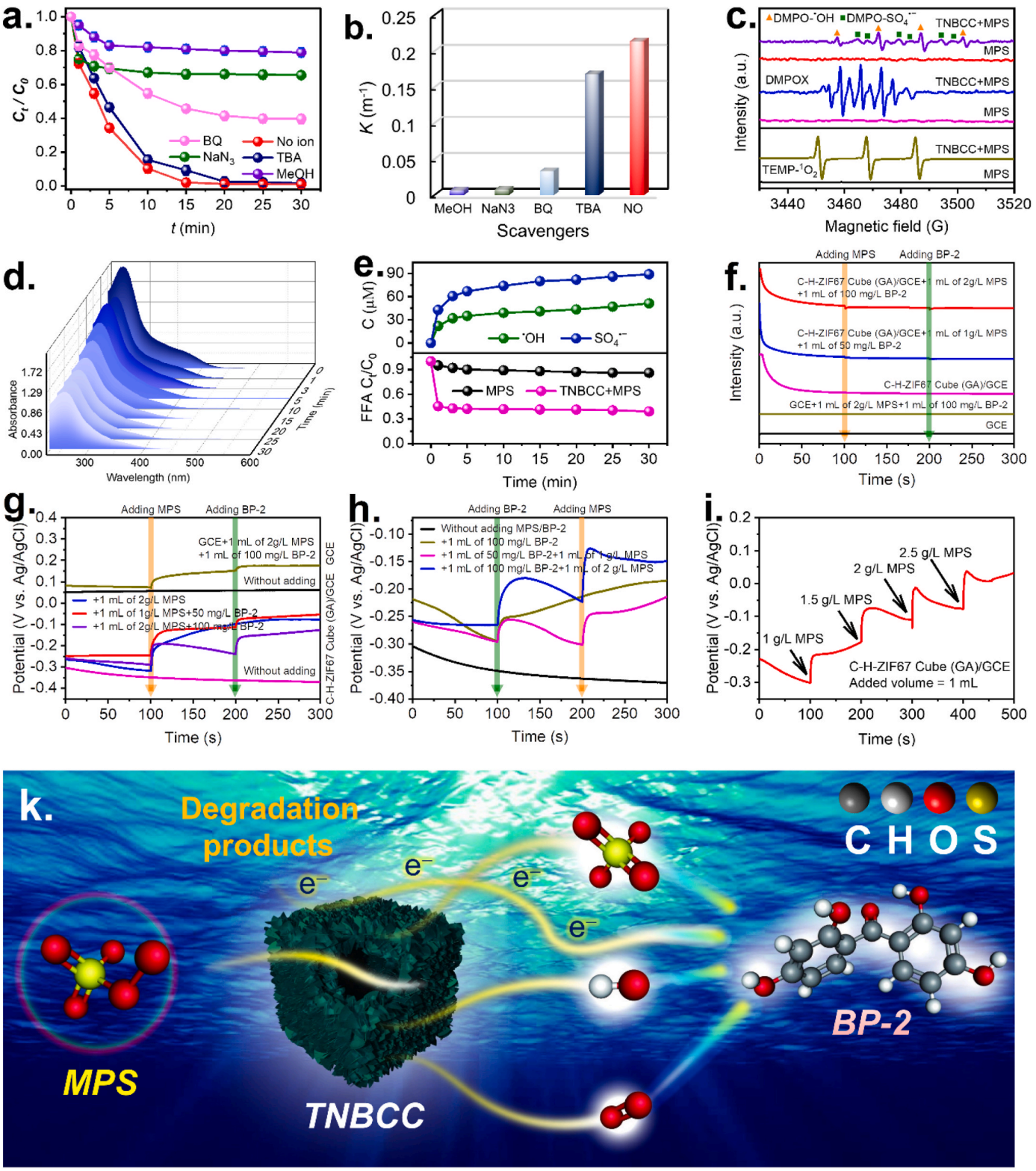

Fig. 5. Effects of ROS probes on degradation of BP-2: (a) degradation curves, (b) rate constants (TNBCC = 25 mg/L, MPS = 200 mg/L, BP-2 = 10 mg/L, TBA = MeOH = 0.1 M, BQ = NaN_3 = 10 mM, and T = 30 °C); (c) EPR analyses; (d) NBT UV–vis spectra (TNBCC = 25 mg/L, MPS = 200 mg/L, NBT = 30 mg/L, and T = 30 °C); (e) quantifications of ROS (TNBCC = 25 mg/L, MPS = 200 mg/L, FFA = 0.75 mM, *p*-HBA = BA = 0.5 mM, and T = 30 °C); (f) current responses of GCE and TNBCC/GCE with and without adding MPS/BP-2; (g, h) OCP curves of GCE and TNBCC/GCE with and without adding MPS/BP-2; (i) changes in potential of TNBCC/GCE with increasing MPS concentration; and (j) illustration of mechanism.

and this phenomenon was consistent to the observation seen in the experiments of scavengers.

Besides, the generation of $^1O_2$ could be quantified by correlating to the consumption of furfuryl alcohol (FFA) through the reaction with $^1O_2$ ($k = 1.2 \times 10^8\ M^{-1}s^{-1}$ (Mostafa and Rosario-Ortiz, 2013)) (Khiem et al., 2023c). Fig. 5(e) shows the FFA consumption at different reaction times in two cases of MPS alone and TNBCC + MPS. One can note that MPS itself without TNBCC would lead to the marginal generation of $^1O_2$. Nonetheless, TNBCC + MPS would cause the consumption of FFA to proceed very quickly, confirming that TNBCC would cause decomposition of MPS as well as induce the formation of $^1O_2$ for degrading BP-2 via the non-radical route.

While these aforementioned results demonstrate that MPS was activated by TNBCC to produce various ROS for degrading BP-2, the interactions between TNBCC, MPS as well as BP-2 shall be further elucidated especially for probing into the electron transport processes. To this end, the relationship of electric current (i) and reaction time (t) of the mixture of TNBCC/MPS/BP-2 was investigated. Firstly, the *i-t* curves in Fig. 5(f) indicates that without the addition of MPS/BP-2, the current of TNBCC/GCE decreased and remained unchanged after 100 s. Nevertheless, a significant drop in the current of the electrode was observed as 1 g/L MPS was added and gradually increased afterwards. The first fall in the current was possibly because of the transfer of electrons from TNBCC/GCE to MPS, thereby redistributing the electron density of TNBCC on GCE, and resulting in the formation of metastable TNBCC/MPS complex (Khiem et al., 2023b). Through this way, MPS was reduced by accepting electrons. This complex was more stable as the current rose up subsequently, implying the partial decomposition of MPS. The succeeding addition of BP-2 decreased the current, meaning that electrons from BP-2 migrated to MPS via TNBCC as an electron mediator, resulting in more MPS decomposition. The current was further decreased to a larger extent as MPS or BP-2 with a higher concentration was added. Compared with sole GCE, the current response of TNBCC/GCE was more obvious, suggesting TNBCC substantially improved electron transfer ability of the electrode.

Besides, the open-circuit potential (OCP) measurement with the addition of MPS/BP-2 would be another evidence for the formation of such metastable TNBCC/MPS complex. As shown in Fig. 5(g), the addition of 1 g/L MPS induced an increase in the potential, indicating MPS combined with TNBCC to form the metastable TNBCC/MPS complex (Khiem et al., 2023b). However, the addition of BP-2 before MPS (Fig. 5(h)) increased the potential to a lesser extent, suggesting the formation of the metastable complex was mainly occurred between TNBCC and MPS. Comparable to the current response, the rise in the potential of TNBCC/GCE (Fig. 5(g)) was also more apparent to that of sole GCE, revealing higher electron transfer capacity of TNBCC. The addition of BP-2 later continued to increase the potential to a higher level (Fig. 5(g)), which was even enhanced as raising the concentration of BP-2 to 100 mg/L. However, the potential did not decrease afterwards, suggesting the BP-2 concentration was still not high enough. This was different from the addition of BP-2 before MPS as shown in Fig. 5(h), where the injection of MPS with a higher concentration decreased the potential after 100 mg/L of BP-2 was added. The fall in the potential manifests that BP-2 concentration was high enough to donate its electrons to TNBCC, leading to consumption of the complex, and thereby decreasing the potential. In addition, the oxidative capacity of TNBCC was further tested by OCP with increasing the concentration of MPS injected. Fig. 5(i) shows that an increase in MPS concentration raised the potential proportionally, demonstrating high sensitivity of TNBCC, or more precisely, its high oxidative capacity towards MPS. Overall, the degradation of BP-2 in TNBCC + MPS relied on both radical route ($^{\bullet}OH$ and $SO_4^{\bullet -}$) and non-radical route ($^1O_2$ and electron transfer) as illustrated in Fig. 5(j).

3.10. Degradation pathway of BP-2 by TNBCC + MPS

As TNBCC effectively activated MPS and enabled efficient BP-2 degradation, it would be critical to further explore BP-2 degradation pathway especially given that no studies of BP-2 degradation had ever been reported so far. For inspecting BP-2 degradation by ROS (e.g., radicals and non-radical), the computational chemistry on the basis of the First-Principle was employed to probe into the molecular susceptibility of BP-2. Specifically, the molecular structure of BP-2 was firstly optimized to afford a geometrically-optimal BP-2 in Fig. 6(a), and its corresponding distribution of the electrostatic potential (ESP) would be depicted in Fig. 6(b), which signifies that the benzene rings of BP-2 both exhibit much higher electron densities, where the electrophilic attack may occur. In addition, Fig. 6(c) and (d) reveal the highest occupied molecular orbital (HOMO) and the lowest unoccupied molecular orbital (LUMO) of BP-2, where the yellow and blue bubbles denote the electron-poor and electron-rich zones of BP-2, correspondingly. These theoretical calculations suggest that the HOMO located in the benzene rings of BP-2 exhibits a high probability of being attacked, especially electrophilic attacks from $^1O_2$ and metastable TNBCC/MPS complex. Thus, the degradation BP-2 might be initiated from the decomposition of the benzene rings of BP-2.

To further elucidate the most possible sites of BP-2 for receiving attacks, the Fukui indices of BP-2 would be determined and listed in Fig. 6 (g). As BP-2 by TNBCC + MPS was ascribed to the radicals and non-radical species, the iso-surfaces of f^- and f^0, representing the non-radical attack and radical attack, are labelled in Fig. 6(e) and (f), respectively. In particular, Fig. 6(e) and (g) indicate that O1, O3, O5, C15, and C16 exhibit the positive and relatively high values. Nevertheless, since O1, O3 an O5 sites are saturated, C15 and C16 would be more probable for receiving the electrophilic attacks. This also confirms that the benzene rings of BP-2 seemed to easily receive the radical attacks.

On the other hand, Fig. 6(f) and (g) displays that C8 and C15 with relatively high f^0 values would exhibit much higher susceptibility to the radical attacks. Given these analyses, BP-2 might be degraded starting from breakage of the benzene rings possibly at C15, C16 and C8.

To propose the potential degradation pathway of BP-2 by TNBCC + MPS, the mass spectrometry of degradation intermediates from BP-2 decomposition was analyzed as shown in Fig. S5 and Table S4. By incorporating those theoretical insights, the degradation pathway of BP-2 by TNBCC + MPS can be then proposed in Fig. 7.

Initially, the benzene rings of BP-2 (m/s = 245) might be firstly attacked to produce M1 and M8, that would be subsequently oxidized through two distinct degradation routes as depicted as the route I and II in Fig. 7, respectively. Via the route I, M1 would be continuously degraded at its residual benzene ring to form M2, which, subsequently, was oxidized to generate M3 molecules by eliminating the ethanol group. Next, M3 might be further decomposed by cutting off the ethane-1,1-diol group to become M4, followed by the additional elimination of methanol group of M4, generating M5. Continuous attacks on the methanol group of M5 would then result in M6 and M7, and finally to carbon dioxide and water.

On the other hand, the route II would proceed by oxidizing M8 via the ring-opening reaction to form M9 as well as M10, which might undergo the further attacks to eliminate the ethanol groups of M9 and M10, affording M11 molecules. The same reaction might be continued to further remove an additional ethanol group from M11 to afford M12. The further elimination of the methanol group of M12 would then generate M13, which was very comparable to M5, and thus M13 might be then oxidized to form M6 and M7, and finally to carbon dioxide and water.

4. Conclusion

Herein, the TNBCC with the hollow-engineered nanostructured

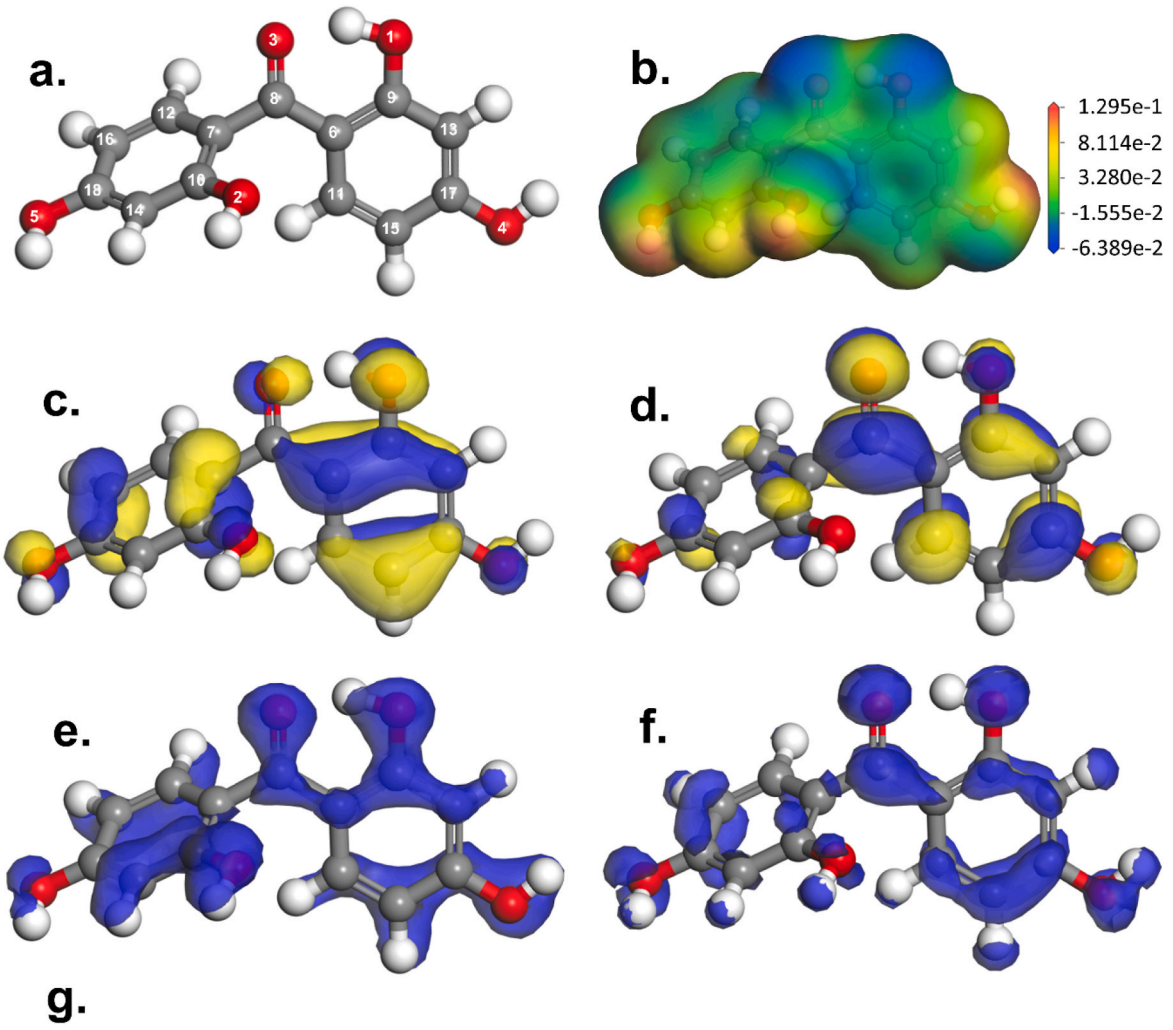

#	1	2	3	4	5	6	7	8	9	10	11	12	13	14	15	16	17	18
Atom	O	O	O	O	O	C	C	C	C	C	C	C	C	C	C	C	C	C
f(-)	**0.09**	0.031	**0.058**	0.049	**0.058**	0.034	0.026	0.019	0.019	-0.002	0.019	0.017	0.033	0.023	**0.059**	**0.042**	0.015	0.023
f(0)	**0.075**	0.012	**0.091**	0.053	0.047	0.013	-0.005	**0.068**	0.028	0.018	0.028	0.012	0.031	0.017	**0.042**	0.029	0.037	0.026
f(+)	0.06	-0.007	0.124	0.056	0.036	-0.008	-0.036	0.116	0.038	0.038	0.038	0.008	0.03	0.011	0.024	0.015	0.058	0.03

Fig. 6. DFT calculation for BP-2: (a) the optimized molecule structure; (b) ESP (isovalue = 0.017); (c) HOMO; (d) LUMO; (e) condensed Fukui index distribution for electrophilic attack (f^-), (f) radical attack (f^0), and (g) a summary of Fukui indices.

cobalt embedded carbon was successfully prepared through the facile but convenient etching treatment using ZIF-67 as a precursor. In comparison to NCCC, the solid (non-hollow) Co@C from the carbonization of ZIF-67, TNBCC, obtained from the etching treatment, possessed not only the unique morphology for improving its textural features, but also advantageous surficial properties of superior electrochemical properties as well as highly reactive surfaces, making TNBCC exhibit the significantly more activities than NCCC and Co_3O_4 for activating MPS in degrading BP-2. Besides, TNBCC + MPS exhibited even lower E_a than other reported studies of degradation of UV absorbers, and remained highly efficiently to eliminate BP-2 in various types of water matrices. More importantly, TNBCC could preserve its structure and catalytic activities over multiple degradation cycles. Mechanisms of BP-2 degradation was unraveled and ascribed to both radical and non-radical routes. These advantageous features make TNBCC a useful activator for MPS to degrade BP-2 and other refractory organic contaminants in water.

Credit author statement

Ta Cong Khiem: Data curation, Writing- Original draft preparation; *Eilhann Kwon*: Data curation, Writing- Original draft preparation; *Jet-Chau Wen*: Data curation; *Nguyen Nhat Huy*: Data curation, Visualization, Investigation; *Tran Doan Trang*: Data curation, *Hou-Chien Chang*: Data curation, Visualization, Investigation; *Xiaoguang Duan*: Writing-Reviewing and Editing; *Chechia Hu*: Data curation, Writing- Original draft preparation; *Kun-Yi Andrew Lin*: Data curation, Writing- Original draft preparation

Declaration of competing interest

The authors declare that they have no known competing financial

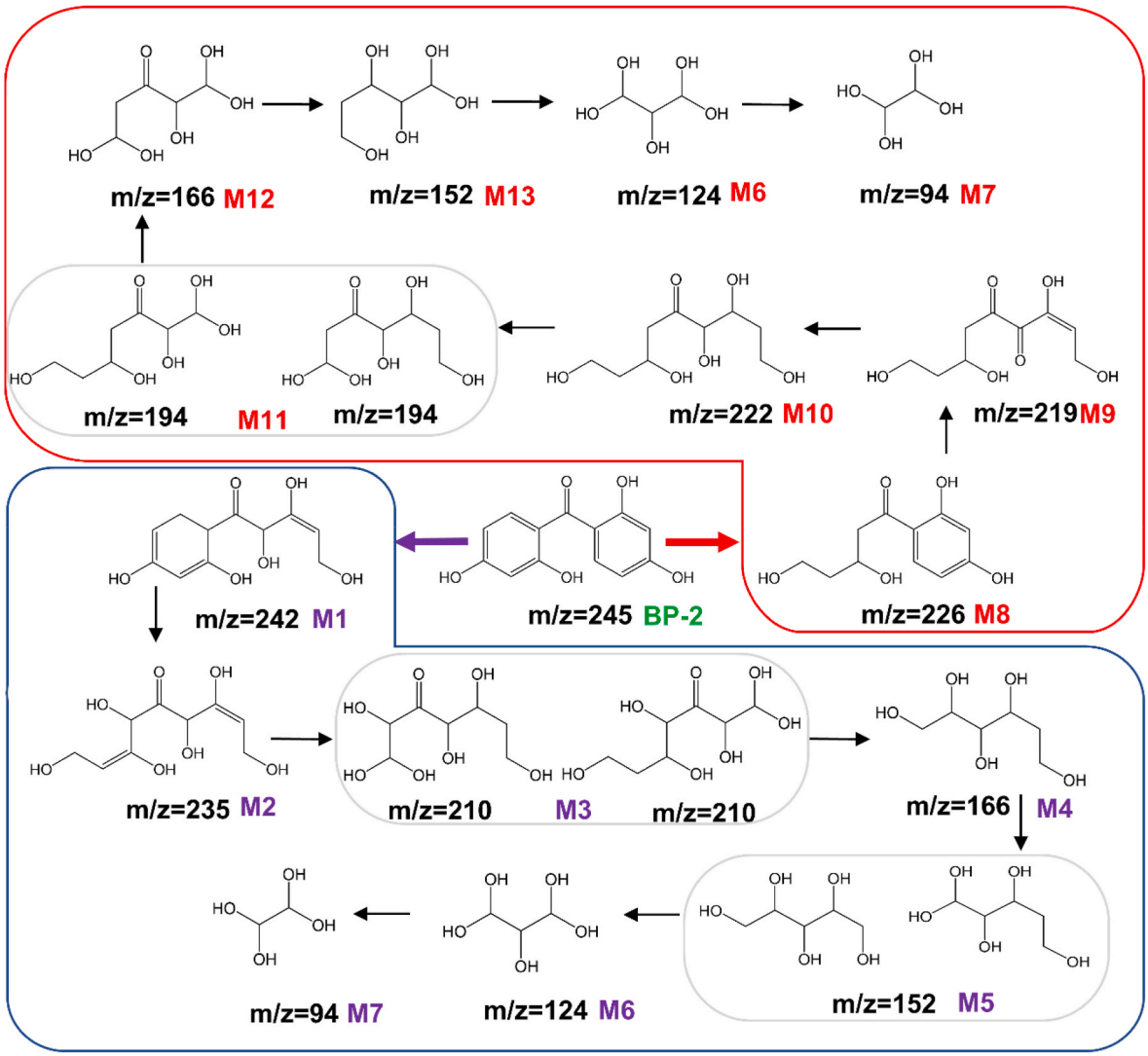

Fig. 7. A proposed degradation process of BP-2 by TNBCC + MPS based on the detected intermediates.

interests or personal relationships that could have appeared to influence the work reported in this paper.

Data availability

The authors are unable or have chosen not to specify which data has been used.

Acknowledgments

This work is supported by the National Science and Technology Council (NSTC-112-2636-E-005-003), Taiwan. The authors gratefully acknowledge the use of SQUID000200 of MOST112-2731-M-006-001 belonging to the Core Facility Center of National Cheng Kung University.

Appendix A. Supplementary data

Supplementary data to this article can be found online at https://doi.org/10.1016/j.chemosphere.2023.138469.

References

Andrew Lin, K.-Y., Chen, B.-C., 2016. Efficient elimination of caffeine from water using Oxone activated by a magnetic and recyclable cobalt/carbon nanocomposite derived from ZIF-67. Dalton Trans. 45, 3541–3551.

Andrew Lin, K.-Y., Hsu, F.-K., Lee, W.-D., 2015. Magnetic cobalt-graphene nanocomposite derived from self-assembly of MOFs with graphene oxide as an activator for peroxymonosulfate. J. Mater. Chem. 3, 9480–9490.

Andrew Lin, K.Y., Chang, H.A., Chen, B.J., 2016. Multi-functional MOF-derived magnetic carbon sponge. J. Mater. Chem. 4, 13611–13625.

Brillas, E., Martínez-Huitle, C.A., 2015. Decontamination of wastewaters containing synthetic organic dyes by electrochemical methods. An updated review. Appl. Catal. B Environ. 166–167, 603–643.

Cao, J., Yang, Z., Xiong, W., Zhou, Y., Wu, Y., Jia, M., Sun, S., Zhou, C., Zhang, Y., Zhong, R., 2020. Peroxymonosulfate activation of magnetic Co nanoparticles relative to an N-doped porous carbon under confinement: boosting stability and performance. Separ. Purif. Technol. 250, 117237.

Chen, H.-H., Park, Y.-K., Kwon, E., Tsang, Y.F., Thanh, B.X., Khiem, T.C., You, S., Hu, C., Lin, K.-Y.A., 2022. Nanoneedle-Assembled Copper/Cobalt sulfides on nickel foam as an enhanced 3D hierarchical catalyst to activate monopersulfate for Rhodamine b degradation. J. Colloid Interface Sci. 613, 168–181.

Chen, X., Chen, X., Yu, E., Cai, S., Jia, H., Chen, J., Liang, P., 2018. In situ pyrolysis of Ce-MOF to prepare CeO2 catalyst with obviously improved catalytic performance for toluene combustion. Chem. Eng. J. 344, 469–479.

Giokas, D.L., Salvador, A., Chisvert, A., 2007. UV filters: from sunscreens to human body and the environment. TrAC, Trends Anal. Chem. 26, 360–374.

Gong, P., Yuan, H., Zhai, P., Xue, Y., Li, H., Dong, W., Mailhot, G., 2015. Investigation on the degradation of benzophenone-3 by UV/H2O2 in aqueous solution. Chem. Eng. J. 277, 97–103.

Guo, W., Su, S., Yi, C., Ma, Z., 2013. Degradation of antibiotics amoxicillin by Co3O4-catalyzed peroxymonosulfate system. Environ. Prog. Sustain. Energy 32, 193–197.

Huang, J., Dai, Y., Singewald, K., Liu, C.-C., Saxena, S., Zhang, H., 2019. Effects of MnO2 of different structures on activation of peroxymonosulfate for bisphenol A degradation under acidic conditions. Chem. Eng. J. 370, 906–915.

Jarry, H., Christoffel, J., Rimoldi, G., Koch, L., Wuttke, W., 2004. Multi-organic endocrine disrupting activity of the UV screen benzophenone 2 (BP2) in ovariectomized adult rats after 5 days treatment. Toxicology 205, 87–93.
Jia, X., Jin, J., Gao, R., Feng, T., Huang, Y., Zhou, Q., Li, A., 2019. Degradation of benzophenone-4 in a UV/chlorine disinfection process: mechanism and toxicity evaluation. Chemosphere 222, 494–502.
Jiang, R., Lu, G., Nkoom, M., Yan, Z., Wu, D., Liu, J., Dang, T., 2020. Mineralization and toxicity reduction of the benzophenone-1 using 2D/2D Cu2WS4/BiOCl Z-scheme system: simultaneously improved visible-light absorption and charge transfer efficiency. Chem. Eng. J. 400, 125913.
Jiang, Z., Lu, W., Li, Z., Ho, K.H., Li, X., Jiao, X., Chen, D., 2014. Synthesis of amorphous cobalt sulfide polyhedral nanocages for high performance supercapacitors. J. Mater. Chem. 2, 8603–8606.
Khiem, T.C., Duan, X., Liu, W.-J., Park, Y.-K., Bui, H.M., Oh, W.-D., Ghotekar, S., Tsang, Y.F., Lin, K.-Y.A., 2023a. MOF-templated hollow cobalt sulfide as an enhanced Oxone activator for degradation of UV Absorber: key role of sulfur Vacancy-Induced highly active CoII sites. Chem. Eng. J. 453, 139699.
Khiem, T.C., Huy, N.N., Kwon, E., Duan, X., Wacławek, S., Bedia, J., Tsai, Y.-C., Ebrahimi, A., Ghanbari, F., Lin, K.-Y.A., 2023b. Hetero-interface-engineered sulfur vacancy and oxygen doping in hollow Co9S8/Fe7S8 nanospheres towards monopersulfate activation for boosting intrinsic electron transfer in paracetamol degradation. Appl. Catalysis B: Environ., 122550
Khiem, T.C., Mao, P.-H., Park, Y.-K., Duan, X., Thanh, B.X., Hu, C., Ghotekar, S., Tsang, Y.F., Lin, K.-Y.A., 2023c. Templating agent-mediated Cobalt oxide encapsulated in Mesoporous silica as an efficient oxone activator for elimination of toxic anionic azo dye in water: mechanistic and DFT-assisted investigations. Chemosphere 313, 137309.
Khiem, T.C., Tuan, D.D., Kwon, E., Huy, N.N., Oh, W.-D., Chen, W.-H., Lin, K.-Y.A., 2022a. Degradation of dihydroxybenzophenone through monopersulfate activation over nanostructured cobalt ferrites with various morphologies: a comparative study. Chem. Eng. J. 450, 137798.
Khiem, T.C., Tuan, D.D., Kwon, E., Thanh, B.X., Tsang, Y.F., Munagapati, V.S., Wen, J.-C., Hu, C., Lin, K.-Y.A., 2022b. Hollow and oval-configured ultrafine Co3O4 as a highly-efficient activator of monopersulfate for catalytic elimination of Azorubin S. Sustain. Environ. Res. 32, 48.
Kim, Y., Ryu, J.C., Choi, H.-S., Lee, K., 2011. Effect of 2,2′,4,4′-tetrahydroxybenzophenone (BP2) on steroidogenesis in testicular Leydig cells. Toxicology 288, 18–26.
Kohantorabi, M., Moussavi, G., Giannakis, S., 2021. A review of the innovations in metal- and carbon-based catalysts explored for heterogeneous peroxymonosulfate (PMS) activation, with focus on radical vs. non-radical degradation pathways of organic contaminants. Chem. Eng. J. 411, 127957.
Lai, H.-K., Chou, Y.-Z., Lee, M.-H., Lin, K.-Y.A., 2018. Coordination polymer-derived cobalt nanoparticle-embedded carbon nanocomposite as a magnetic multi-functional catalyst for energy generation and biomass conversion. Chem. Eng. J. 332, 717–726.
Li, B.-C., Yang, H., Kwon, E., Dinh Tuan, D., Cong Khiem, T., Lisak, G., Xuan Thanh, B., Ghanbari, F., Andrew Lin, K.-Y., 2021. Catalytic reduction of bromate by Co-embedded N-Doped carbon as a magnetic non-noble metal hydrogenation catalyst. Sep. Purif. Technol., 119320
Li, Y., Li, F.-M., Meng, X.-Y., Li, S.-N., Zeng, J.-H., Chen, Y., 2018. Ultrathin Co3O4 nanomeshes for the oxygen evolution reaction. ACS Catal. 8, 1913–1920.
Lin, K.-Y.A., Chang, H.-A., Chen, R.-C., 2015. MOF-derived magnetic carbonaceous nanocomposite as a heterogeneous catalyst to activate oxone for decolorization of Rhodamine B in water. Chemosphere 130, 66–72.
Lin, K.-Y.A., Lin, J.-T., Lu, X.-Y., Hung, C., Lin, Y.-F., 2017. Electrospun magnetic cobalt-embedded carbon nanofiber as a heterogeneous catalyst for activation of oxone for degradation of Amaranth dye. J. Colloid Interface Sci. 505, 728–735.
Lin, X.-R., Kwon, E., Hung, C., Huang, C.-W., Oh, W.D., Lin, K.-Y.A., 2021. Co3O4 nanocube-decorated nitrogen-doped carbon foam as an enhanced 3-dimensional hierarchical catalyst for activating Oxone to degrade sulfosalicylic acid. J. Colloid Interface Sci. 584, 749–759.
Liu, B., Li, C., Zhang, G., Yao, X., Chuang, S.S.C., Li, Z., 2018. Oxygen vacancy promoting dimethyl carbonate synthesis from CO2 and methanol over Zr-doped CeO2 nanorods. ACS Catal. 8, 10446–10456.
Liu, H., Sun, P., Feng, M., Liu, H., Yang, S., Wang, L., Wang, Z., 2016. Nitrogen and sulfur co-doped CNT-COOH as an efficient metal-free catalyst for the degradation of UV filter BP-4 based on sulfate radicals. Appl. Catal. B Environ. 187, 1–10.
Liu, M., Wu, N., Tian, B., Zhou, D., Yan, C., Huo, Z., Qu, R., 2022a. Experimental and theoretical study on the degradation of Benzophenone-1 by Ferrate (VI): new insights into the oxidation mechanism. J. Hazard Mater. 425, 127877.
Liu, W.-J., Kwon, E., Huy, N.N., Khiem, T.C., Lisak, G., Wi-Afedzi, T., Wu, C.-C., Ghanbari, F., Lin, K.-Y.A., 2022b. Facilely-prepared sulfide-doped Co3O4 nanocomposite as a boosted catalyst for activating Oxone to degrade a sunscreen agent. J. Taiwan Inst. Chem. Eng. 133, 104253.
Liu, W.-J., Kwon, E., Thanh, B.X., Khiem, T.C., Lisak, G., Lee, J., Lin, K.-Y.A., 2022c. 3D hexagonal hierachitectured cobalt sulfide as an enhanced catalyst for activating monopersulfate to degrade sunscreen agent ensulizole. J. Taiwan Inst. Chem. Eng. 131, 104109.
Liu, W.-J., Kwon, E., Thanh, B.X., Lee, J., Ta, C.K., Sirivithayapakorn, S., Lin, K.-Y.A., 2022d. Nanoscale CoNi alloy@ carbon derived from Hofmann-MOF as a magnetic/effective activator for monopersulfate to eliminate an ultraviolet filter. J. Nanostruct. Chem. 1–14.
Liu, W.-J., Kwon, E., Xuan Thanh, B., Cong Khiem, T., Dinh Tuan, D., Lin, J.-Y., Wi-Afedzi, T., Hu, C., Sirivithayapakorn, S., Lin, K.-Y.A., 2022e. Hofmann-MOF derived nanoball assembled by FeNi alloy confined in carbon nanotubes as a magnetic catalyst for activating peroxydisulfate to degrade an ionic liquid. Sep. Purif. Technol. 295, 120945.
Liu, W.-J., Park, Y.-K., Bui, H.M., Huy, N.N., Lin, C.-H., Ghotekar, S., Wi-Afedzi, T., Lin, K.-Y.A., 2023. Hofmann-MOF-derived CoFeNi nanoalloy@ CNT as a magnetic activator for peroxymonosulfate to degrade benzophenone-1 in water. J. Alloys Compd. 937, 165189.
Liu, W.-J., Park, Y.-K., Chen, W.-H., Bui, H.M., Munagapati, V.S., Tuan, D.D., Wen, J.-C., You, S., Da Oh, W., Lin, K.-Y.A., 2022f. Highly-efficient degradation of ensulizole using monopersulfate activated by nanostructured cobalt oxide: a comparative study on effects of different nanostructures. J. Environ. Chem. Eng. 10, 107137.
Liu, W.-J., Yang, H., Park, Y.-K., Kwon, E., Huang, C.-W., Thanh, B.X., Khiem, T.C., You, S., Ghanbari, F., Lin, K.-Y.A., 2022g. Enhanced degradation of ultra-violet stabilizer Bis (4-hydroxy) benzophenone using oxone catalyzed by hexagonal nanoplate-assembled CoS 3-dimensional cluster. Chemosphere 288, 132427.
Ma, Y., Du, K., Guo, Y., Tang, M., Yin, H., Mao, X., Wang, D., 2022. Electrolytic core–shell Co@ C for diethyl phthalate degradation. Chem. Eng. J. 431, 134065.
Madihi-Bidgoli, S., Asadnezhad, S., Yaghoot-Nezhad, A., Hassani, A., 2021. Azurobine degradation using Fe2O3@multi-walled carbon nanotube activated peroxymonosulfate (PMS) under UVA-LED irradiation: performance, mechanism and environmental application. J. Environ. Chem. Eng. 9, 106660.
Mao, P.-H., Khiem, T.C., Kwon, E., Chang, H.-C., Bui, H.M., Duan, X., Yang, H., Ghotekar, S., Chen, W.-H., Tsai, Y.-C., 2022. Ambient-Visible-light-Mediated enhanced degradation of UV stabilizer bis (4-hydroxyphenyl) methanone by nanosheet-assembled cobalt titanium oxide: a comparative and DFT-assisted investigation. Water 14, 3318.
Miao, J., Geng, W., Alvarez, P.J.J., Long, M., 2020. 2D N-doped porous carbon derived from polydopamine-coated graphitic carbon nitride for efficient nonradical activation of peroxymonosulfate. Environ. Sci. Technol. 54, 8473–8481.
Mostafa, S., Rosario-Ortiz, F.L., 2013. Singlet oxygen formation from wastewater organic matter. Environ. Sci. Technol. 47, 8179–8186.
Nguyen, H.T., Lee, J., Kwon, E., Lisak, G., Thanh, B.X., Oh, W.D., Lin, K.-Y.A., 2021. Metal-complexed covalent organic frameworks derived N-doped carbon nanobubble–embedded cobalt nanoparticle as a magnetic and efficient catalyst for oxone activation. J. Colloid Interface Sci. 591, 161–172.
Silvia Díaz-Cruz, M., Llorca, M., Barceló, D., Barceló, D., 2008. Organic UV filters and their photodegradates, metabolites and disinfection by-products in the aquatic environment. TrAC, Trends Anal. Chem. 27, 873–887.
Trang, N.H., Kwon, E., Lisak, G., Hu, C., Andrew Lin, K.Y., 2021. Cobalt ferrite nanoparticle-loaded nitrogen-doped carbon sponge as a magnetic 3D heterogeneous catalyst for monopersulfate-based oxidation of salicylic acid. Chemosphere 267.
Tuan, D.D., Chang, F.-C., Chen, P.-Y., Kwon, E., You, S., Tong, S., Lin, K.-Y.A., 2021. Covalent organic polymer derived carbon nanocapsule–supported cobalt as a catalyst for activating monopersulfate to degrade salicylic acid. J. Environ. Chem. Eng. 9, 105377.
Tuan, D.D., Hung, C., Da Oh, W., Ghanbari, F., Lin, J.-Y., Lin, K.-Y.A., 2020a. Porous hexagonal nanoplate cobalt oxide derived from a coordination polymer as an effective catalyst for activating Oxone in water. Chemosphere 261, 127552.
Tuan, D.D., Khiem, C., Kwon, E., Tsang, Y.F., Sirivithayapakorn, S., Thanh, B.X., Lisak, G., Yang, H., Lin, K.-Y.A., 2022a. Hollow porous cobalt oxide nanobox as an enhanced for activating monopersulfate to degrade 2-hydroxybenzoic acid in water. Chemosphere 294, 133441.
Tuan, D.D., Kwon, E., Phattarapattamawong, S., Thanh, B.X., Khiem, T.C., Lisak, G., Wang, H., Lin, K.-Y.A., 2022b. Nitrogen-containing carbon hollow nanocube-confined cobalt nanoparticle as a magnetic and efficient catalyst for activating monopersulfate to degrade a UV filter in water. J. Environ. Chem. Eng. 10, 106989.
Tuan, D.D., Liu, W.-J., Kwon, E., Thanh, B.X., Munagapati, V.S., Wen, J.-C., Lisak, G., Hu, C., Lin, K.-Y.A., 2022c. Ultrafine cobalt nanoparticle-embedded leaf-like hollow N-doped carbon as an enhanced catalyst for activating monopersulfate to degrade phenol. J. Colloid Interface Sci. 606, 929–940.
Tuan, D.D., Oh, W.D., Ghanbari, F., Lisak, G., Tong, S., Andrew Lin, K.-Y., 2020b. Coordination polymer-derived cobalt-embedded and N/S-doped carbon nanosheet with a hexagonal core-shell nanostructure as an efficient catalyst for activation of oxone in water. J. Colloid Interface Sci. 579, 109–118.
Wang, B., Yang, L., Yuan, F., Zhang, D., Wang, H., Wang, Q., Sun, H., Li, Z., Sun, H., Li, W., 2023. Chemical-etching strategy tailoring hollow carbon confined highly dispersed CoP nanoparticles for durable potassium storage. Electrochim. Acta 439, 141681.
Wang, Q., Liu, C., Zhou, D., Chen, X., Zhang, M., Lin, K., 2022a. Degradation of bisphenol a using peroxymonosulfate activated by single-atomic cobalt catalysts: different reactive species at acidic and alkaline pH. Chem. Eng. J. 439, 135002.
Wang, S., Wang, J., 2021. Degradation of sulfamethoxazole using peroxymonosulfate activated by cobalt embedded into N, O co-doped carbon nanotubes. Separ. Purif. Technol. 277, 119457.
Wang, Y., Wang, Y., Liu, Y., 2022b. Fe2+/heat-coactivated PMS oxidation-absorption system for H2S removal from gas phase. Separ. Purif. Technol. 286, 120458.
Wei, Q., Liu, T., Wang, Y., Dai, L., 2019. Three-dimensional N-doped graphene aerogel-supported Pd nanoparticles as efficient catalysts for solvent-free oxidation of benzyl alcohol. RSC Adv. 9, 9620–9628.
Wen, Y., Sharma, V.K., Ma, X., 2022. Activation of peroxymonosulfate by phosphate and carbonate for the abatement of atrazine: roles of radical and nonradical species. ACS ES&T Water 2, 635–643.
Xue, Y., Pham, N.N.T., Nam, G., Choi, J., Ahn, Y.-Y., Lee, H., Jung, J., Lee, S.-G., Lee, J., 2021. Persulfate activation by ZIF-67-derived cobalt/nitrogen-doped carbon composites: kinetics and mechanisms dependent on persulfate precursor. Chem. Eng. J. 408, 127305.

Yin, J.-Y., Da Oh, W., Kwon, E., Thanh, B.X., You, S., Wang, H., Lin, K.-Y.A., 2021a. Cobalt sulfide nanofilm-assembled cube as an efficient catalyst for activating monopersulfate to degrade UV filter, 4, 4′-dihydroxybenzophenone, in water. Colloids Surf. A Physicochem. Eng. Asp. 625, 126891.

Yin, J.-Y., Wang, H., Yu, K.-P., Lee, J., Lin, K.-Y.A., 2021b. Degradation of sunscreen agent 2-phenylbenzimidazole-5-sulfonic acid using monopersulfate activated by MOF-derived cobalt sulfide nanoplates. J. Water Proc. Eng. 44, 102282.

Zhang, B.-T., Zhang, Y., Teng, Y., Fan, M., 2015. Sulfate radical and its application in decontamination technologies. Crit. Rev. Environ. Sci. Technol. 45, 1756–1800.

Zhang, B., Han, Z., Xin, Y., Zhang, Y., Li, W., Li, B., Ding, A., Ma, J., He, X., 2022. Peroxymonosulfate activation by vacuum ultraviolet and trace copper ions: a new way to boost Cu(II)/Cu(I) redox cycle. Chem. Eng. J. 450, 138097.

Zhang, T., Chen, Y., Wang, Y., Le Roux, J., Yang, Y., Croué, J.-P., 2014. Efficient peroxydisulfate activation process not relying on sulfate radical generation for water pollutant degradation. Environ. Sci. Technol. 48, 5868–5875.

Zhou, Y., Jiang, J., Gao, Y., Ma, J., Pang, S.-Y., Li, J., Lu, X.-T., Yuan, L.-P., 2015. Activation of peroxymonosulfate by benzoquinone: a novel nonradical oxidation process. Environ. Sci. Technol. 49, 12941–12950.

Zhu, K., Xia, W., He, D., Huang, J., He, H., Lei, L., Chen, W., Liu, X., 2022. Facile fabrication of Fe/Fe3C embedded in N-doped carbon nanofiber for efficient degradation of tetracycline via peroxymonosulfate activation: role of superoxide radical and singlet oxygen. J. Colloid Interface Sci. 609, 86–101.